ABSTRACT

TUNG, MOUDA. In-situ Electron Monitoring for the Electron Beam Melting Process (Under the direction of Dr. Timothy Horn).

Metal additive manufacturing process (AM) had been applied in the production of highly customized or geometrically complex components such as medical and aerospace applications. Yet some major issues in the robustness and stability of the process still persist in commercially available solutions, with limitations to its surface finish, tolerances, and repeatability. The ability to closely monitor the observable process signatures that links to defect formation is crucial to the ultimate goal of realtime parameter adjustments. Process-induced porosity defects such as lack of fusion, trapped gas, and keyhole formations, as well as warpage and deleterious phases in the resulting parts can all be mitigated through changes in melt pattern, beam focus, and beam current, etc. In-situ sensing methods used in EBM are limited to its vacuum and high temperature environment and active sensing methods used in selective laser melting (SLM) are not applicable. Visible and IR optics are the most common way to monitor the condition of the build, but these along with pyrometry measurements require access of a direct line of sight to the build platform, which a commercial ARCAM system does not provide. Even with the necessary modifications to support such monitoring hardware the optical path must be protected against metal vapor condensation, plus all available methods are off axis and are subjected to thermionic influence of the gun.

The emerging electron imaging technique incorporated the principles associated with scanning electron microscopy (SEM), the same had been incorporated in the control system in the EB welding industry. Commercially available EB welding electron gun with a backscattered electron detector attachment, as well as modified ARCAM A1 heatshield were first experimented. The former demonstrated the ability to detect process-induced open porosity using

a post-melt layer scan of the surface, while the latter benchmarked the resolution possible using a generic detector design with the least amount of intrusion compared with optical alternatives. The possibility of using such monitoring mechanism during the melting process of the EBM was eluded to in the following previous work, while the effect of plate temperature has been demonstrated to do little effect to the overall detector's functionality.

The focus of this research is to first build a similar detector hardware and improve upon the design, as well as demonstrate the melt process monitoring capability while using the acquired information to assist the research into novel material AM parameter development. An electron detection and imaging system was developed around the ARCAM EBM system using data acquisition (DAQ) system form National Instruments and imaging software written in Python, and is demonstrated to be capable of performing post-melt layer imaging that is comparable to the ARCAM's LayerQam optical imaging system. The system is also employed during the melting process, where a DOE build for pure copper with known porosity-inducing parameters are used. The resulting process-induces open porosity of the surface are shown to be indicative of the porosity defects within the sample parts examined using optical microscopy.

In-situ Electron Imaging for the Electron Beam Melting Process

by

Mouda Tung

A thesis submitted to the Graduate Faculty of
North Carolina State University
in partial fulfillment of the
requirements for the degree of
Master of Science

Industrial Engineering

Raleigh, North Carolina
2019

APPROVED BY:

_____	_____
Dr. Timothy Horn Committee Chair	Dr. Christopher Rock
_____	_____
Dr. Victoria Miller	Dr. Russell King

BIOGRAPHY

Mouda Tung was born in Taipei, Taiwan in 1993. Complete his Bachelor of Engineering for National Taiwan Normal University in 2015. Working as a Graduate research Assistant in the Center for Additive Manufacturing and Logistics from May of 2018 to August of 2019. Electronic hobbyist and space enthusiast.

ACKNOWLEDGMENTS

This work has been funded in part by the Center for Additive Manufacturing and Logistics and the NAVAL Sea Systems Command.

TABLE OF CONTENTS

LIST OF TABLES

LIST OF FIGURES

CHAPTER 1: Introduction

Metal additive manufacturing process (AM) has been applied in the production of highly customized or geometrically complex components for applications such as medical and aerospace, due to its ability of producing complex geometries. Yet some major issues in the robustness and stability of the process still persist in commercially available solutions (Everton et al 2016, Sames et al 2016), with limitations to its surface finish, tolerances, and repeatability. The ability to closely monitor the observable process signatures that links to defect formation is crucial to the ultimate goal of producing defect-free parts them through real time parameter adjustments common in closed-loop systems. Process-induced porosity defects such as lack of fusion, trapped gas, and keyhole formations (Grasso and Colosimo, 2017), as well as warpage and deleterious phases in the resulting parts can all be mitigated through changes in melt pattern, beam focus, and beam current, etc. (Sharratt, 2015, Prabhakar *et al,* 2015) The studies of Sames *et al* (2016) and a report of the National Institute of Standard and Technology (NIST) (Mani *et al,* 2015) included a survey of metal AM processing defects. In-situ sensing methods used in EBM are typically constrain due to its vacuum and high temperature environment and active sensing methods used in selective laser melting (SLM) are not applicable, as the electron components cannot withstand its processing environment. Visible and IR optics are the most common methods to monitor the condition of the build (Gong *et al*., 2013, Rodriguez *et al*., 2012, Mireles *et al*., 2015, Boone *et al.,* 2018), but these along with pyrometry measurements require access of a direct line of sight to the build platform, which a commercial ARCAM system does not provide (ARCAM A2 manual). Even with the necessary modifications to support such monitoring hardware the optical path must be protected against metal vapor condensation, plus all available methods are off axis and are subjected to thermionic influence of the gun (Wong *et al.,* 2018).

The emerging electron imaging technique was first experimented by Wong *et al.* (2018) and Arnold *et al.* (2018) incorporated the principle of scanning electron microscopy (SEM), by collecting electrons ejected of the build during a low current scan, incorporated in the control system in the EB welding industry starting in the early 1980's (ref). Arnold *et al.* (2018) used a commercially available EB welding electron gun with a backscattered electron detector attachment, whereas Wong *et al.* (2018) modified an ARCAM A1 heatshield into an electron detector. The former demonstrated the ability to detect process-induced open porosity using a post-melt layer scan of the surface, while the latter benchmark the resolution possible using a generic detector design with a less amount of intrusion compared with optical alternatives. The possibility of using such monitoring technology during the melting was eluded to in subsequent work by Wong *et al.* (2019) where the effect of plate temperature has demonstrated to do little effect to the overall detector's functionality.

The focus of this research is to first build the same custom detector hardware and improve upon the design, as well as demonstrate the melt process monitoring capability while using the acquired information to assist the research into novel material AM parameter development. In order achieve the primary goal of this study a similar setup of the prototyping electron imaging apparatus was setup on the ARCAM A2, and with a slightly varied heatshield modification as well as data acquisition method compared with previous studies; Chapter 2 would first examine the in-situ monitoring methods currently in used in powder bed AM systems; Chapter 3 will review the principle pf electron detection and the physics of electron gun, follow by outlining the development of the electron monitoring/imaging hardware and the necessary software infrastructure, as well as the results for the initial test on the technology; Chapter 4 explore the possibility of using the beam speed derived from beam location to assist the parameter

development of high purity copper, as well as performing in-situ melt monitoring to generate melt surface images.

CHAPTER 2: Review of Process Monitoring Methods in Electron Beam Melting Powder Bed AM

Electron Beam Melting is a powder bed fusion (PBF) process categorized by ISO/ASTM standard 52900:2015 as a recognized approach for producing metallic components by additive manufacturing. Figure 2.1 shows an illustration of a generic powder bed AM system. These systems process a relatively thin layer of metallic powder, ranging in size typically from 10-100 microns, is spread onto a substrate, or previously created bed of powder, most commonly by a rake blade. However, alternative methods of bed formation have also been demonstrated. Subsequently, a focused energy source, most often an IR laser or an electron beam, is selectively scanned over the surface of the powder bed within geometric bounds based upon the cross-sectional geometry of the desired component. The platform is then lowered a predetermined increment (e.g. 20µm, 50 µm), and the process is repeated.

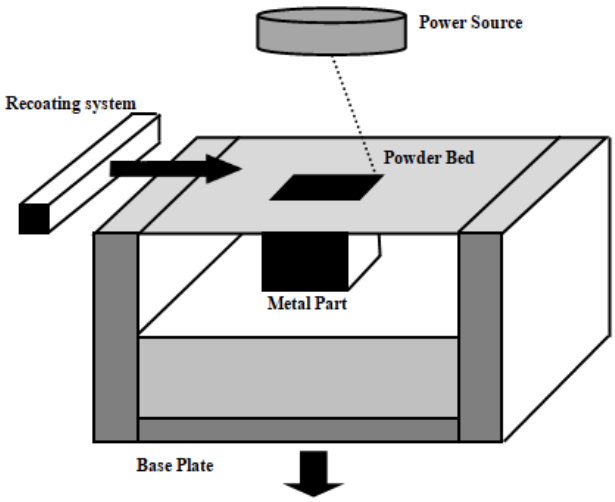

Figure 2.1: Illustration of a generic powder bed AM system.

A key difference between laser and electron beam-based PBF systems is the operating environment. Laser PBF systems typically operate in an environment which can either be inert, e.g. He, N, Ar, etc. or reactive, e.g. H, CO_2, CO, O, SF_6, and the optical deflection system consists of lenses difficult to operate under vacuum, as it would be subjected to metallization. EBM based processes, by contrast, must operate in a medium vacuum environment of around 10^{-2} to 10^{-6} mBar. The EBM system had the advantage of higher wattage and capable of delivering more power to the powder bed surface, although the advancement in the development of laser systems are approaching comparable power output.

To deliver the power needed for melting the metal powder laser systems uses a series of lances to direct the beam whereas EBM uses electromagnetic lenses to perform the same task, illustrated in Figure 2.2. The presence of physical lenses presents difficult for laser systems to operate at vacuum environment for prolong period, due to metal condensation on the lenses. On top of all, the wavelength for which each system operates represent their respective range of process efficiency considering the absorptivity of different materials (Romano, 2015).

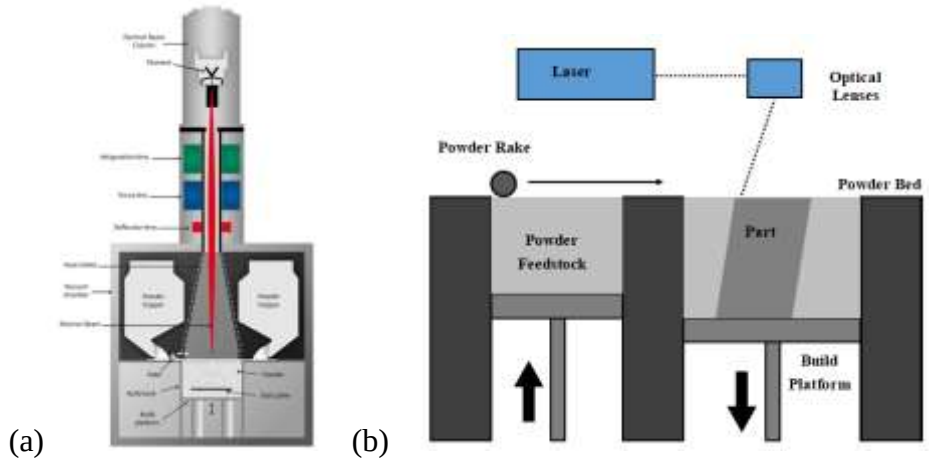

Figure 2.2. (a) Schematic EBM setup from ARCAM AB, (b) Schematic of the DMLS system

Ultimately, both processes achieve the same goal of making solid components by adjusting the processing parameter, these include the preheat temperature, beam diameter, scan speed, layer thickness, powder particle size, and beam power, etc. Higher preheat temperature lead to less dramatic cooling and facilitates equiaxed grain microstructures (Larosa *et al.*, 2014). Smaller particle size particles and denser packing results in heat being better transferred through the powder into lower levels, leads to lower temperatures and quicker cooling. This also means denser built parts in sintering and it also means shallower melt pools in melting. Beam diameter, scan speed, and power affects the amount of energy input in a local patch of powder material, leads to variations in temperature, penetration depth, and cooling rate (Shen and Chou, 2012).

A myriad of factors influence variation in part quality during powder bed AM, from variations in microstructure to process and material induced defects, to geometric errors. Direct observation of these factors and the phenomena that give rise to them has been the hallmark of common approaches to process monitoring in AM. This has traditionally been challenging in EBM based processes, where the comparatively high temperatures, vacuum environment, and condensation of metal vapors complicate the utilization of the monitoring techniques commonly used in laser PBF (e.g visible/near IR/IR imaging and infrared optics, acoustic emissions, light interferometry, etc.).

2.1 EBM defects and their causes

Reports by Sharratt (2015), Grasso and Colosimo (2017) summarized the defects in metal AM into the following defects: (1) equipment, (2) process, (3) design and (4) feedstock material. This section will be devoted to the discussion of some of the major process related defects, follow by the monitoring methods that targeted to mitigate them.

2.1.1 Porosity

Porosity is a common process induce defect in metal 3D printing, and can be attributed to three major causes: 1) A lack of energy input, causing “Lack of fusion porosity”, 2) A surplus of energy input, causing “keyholes porosity”, and 3) Residual trap gas porosity (Gong et al. 2014, King et al. 2015). Lack of fusion is the result of incomplete welding of layers or adjacent melt pools, resulting in an irregular morphology (Tammas-Williams et al, 2015) and have been reported to become more common as the ratio of power over velocity decreases. (Puebla et al. 2012). Keyhole porosity from elongation of the melt pool under high energy conditions. Figure 2.3. illustrates the formation of a thin, tubular structure, with a pocket geometry at the bottom.

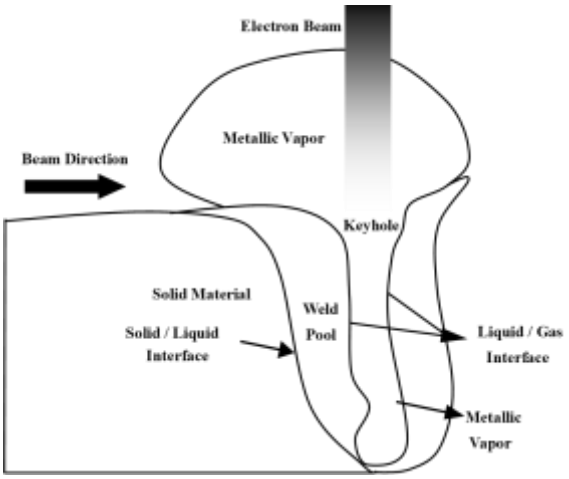

Figure 2.3. The schematic of vacuum electron beam welding process.

Studies involved using synchrotron X-ray to image the condition of a laser systems melt pool was done by Zhao and others (Zhao et al., 2017). Utilizing a high-speed, hard X-ray from a photon source (shown in Figure 2.4). A single melt track of powder from the side while a laser source on top of the powder performs the scan, with the diffraction and imaging detector place downstream of the photon source. The formation process of the keyhole pore was observed deep under the base metal and it has revealed that the closure of keyholes took less than 50μs, and that the void generated deep under the surface was pinned by the advance solidification front in the leading edge of the beam.

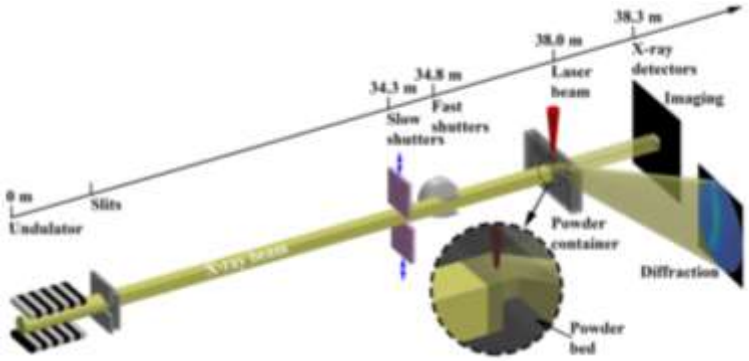

Figure 2.4. Schematic of the high-speed X-ray imaging and diffraction experiments on laser powder bed fusion process at the 32-ID-B beamline of the Advanced Photon Source (Zhao et al., 2017)

Trap gas porosities in the EBM process are traces of gas left in the powder feedstock during the atomization stage when they're manufactured, which are very hard to eliminate due to the rate of solidification. Methods such as suppressing the entrapment of atomization gas during the powder making process would help to mitigate the amount of trapped gas but requires the use of an alternate atomization mechanism, as the lower energy can avoid the "bag breakup and collapse" process described by Rabin et al. (1990).

2.1.2 Geometric Defects and Deformation

EBM manufactured parts may exhibit different types of dimensional and geometric deviations from the nominal model. Mousa (2016) investigated the curling phenomenon, i.e. a combination of shrinking and warping that yields a curved profile of down-facing surfaces intended to be flat. Curling is usually associated with an uneven shrinkage between the top and the bottom of the part. Warping is due to the thermal stress formed by the rapid solidification during AM process, as the temperature gradient leads to the differences in thermal expansion within the formed parts (Vo *et al*. 2018). Another kind of geometrical distortion observed and investigated by different authors is rough surfaces of as-formed layers (Yasa *et al*, 2009, Kleszczynski *et al*, 2012). This combine with the curling may interfere with powder spreading and bed uniformity is successive layers. Another potential geometric defect in EBM is that the beam deflection system may be affected by external magnetic influences, which can change the beam path and shape of the beam, resulting in defected geometrical part defects. This type of can be resolved by isolating the machine from nearby electrical and magnetic sources.

2.1.3 Microstructure and Anisotropy

A common microstructure feature observed in metal AM parts is columnar grain morphology (Kok et al, 2018). These columnar grains are typically aligned parallel to the build direction and caused by the solidification condition common in metal AM. (shown in Figure 2.5). Re-melting of previous layers during the material deposition process would create epitaxial columnar grain growth while provide sufficient thermal gradient within the melt pool, which would prevent nucleation ahead of the solidification front (Dehoff *et al.*, 2015). Traditionally, build orientation adjustments and specifying a minimum cross-sectional thickness were ways to reduce the effect

of the anisotropy and heterogeneity in material properties. Meanwhile literatures have shown that altering the scan strategy across layers is able to control the formation of either equiaxed or columnar grains (Dehoff *et al.,* 2015, Helmer *et al.,* 2016), to differences in the overall direction of the thermal gradient (Ishimoto *et al.,* 2016, Thijs *et al.*, 2013), as well as the use of in-situ printed heat sink to manipulate it (Jamshidinia, 2015).

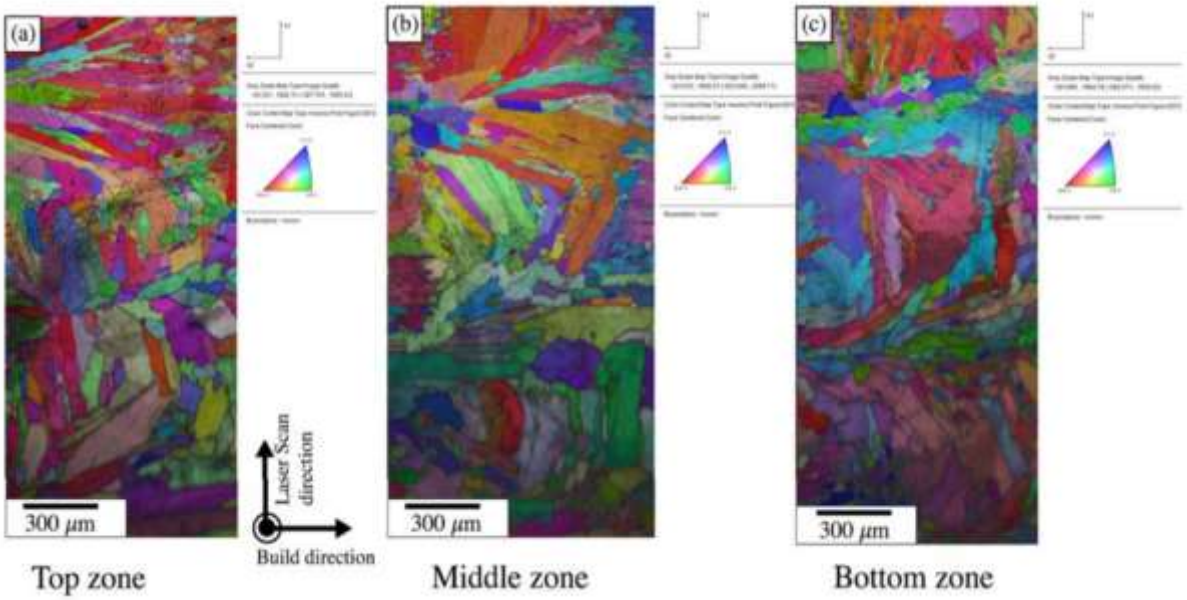

Figure 2.5. Inverse pole figures of samples fabricated using the line scan mode (a) Corresponds to the top zone of the build (b) corresponds to the middle zone and (c) corresponds to the bottom zone (Raghavan et al., 2018).

2.2 In-situ Sensing

Mani *et al.* (2015) at NIST define the variables that can dictate the outcome of the AM process as "process signatures". These are the dynamic characteristics of the powder heating, melting, and solidification processes as they occur during the build which can be categorized into observable and derived signatures. The former can be observed and measured during the process by using in situ sensing devices while the latter can be determined through analytical models or simulations. The following review is focused on the in situ sensing and monitoring approaches used in the electron beam system; Laser systems will not be discussed in detail here but may share some technologies with additions of active sensing methods due to the atmospheric environment.

2.2.1 Visible Wavelength Imaging

Visible wavelength imaging is currently being implemented widely for the powder spreading condition of EBM systems. ARCAM uses a preoperatory camera system to image post rake and melt at each layer for quality control during building. This information can be correlated with microstructure and defects in post-processing analysis, however, is not used for closed loop control (ref ref ref). Other studies have used high-speed camera to validate the beam velocity to calculate the solidification time of the microstructure (Zhang *et al*., 2018). Laser systems allow for a more intricate camera system for process monitoring. And the earliest in-situ monitoring studies were published by several groups (Kruth *et al*., 2007 and Doubenskaia *et al*.,2010). These researches use a coaxially mounted camera pyrometer to investigate the melt pool shape and temperature. Further coaxial monitoring was investigated by Lane, Grantham, and others at NIST (Lane *et al*., 2016), using a series of lances to achieve diffraction-limited imaging with 1:1 magnification in one direction as well as a focused laser beam at 1070 nm in the opposite

direction. Images processed from the data produced has a resolution down to 1.67μm, which is suitable to detect most defects produced by current metal AM systems (Lane *et al*., 2017).

To monitor the melt pool Craeghs *et al*. (2012) experimented with an integrated optical setup that allows the position of the laser relative to the powder bed to be logged in tandem with the melt pool data. The data from the individual melt pool were processed into a greyscale map of the part, to resolved part overheating, porosity, and "balling" of the melt pool. Many reports have used high-speed imaging in metal AM to measure a verity of melt pool phenomena. Furomoto *et al*. (2012) experiment with an in-line melt monitoring system using a high-speed camera assembled vertically above the powder bed to observe the condition of the metal powder during irradiation, illuminated by a metal halide lamp. A similar setup has been used to observe the melt pool formation and spatters in several (Gunenthiram *et al*., 2017, Ly *et al*., 2017, Khairallah *et al*., 2016, and Haehnel and Dade, 2008), which may lead to defects in metal AM parts. These include recoil pressure build-up by the metal vaper within the melt pool, Marangoni effect that causes convection flow within the melt pool, shown in Figure 2.2. (b), and vaper jet entrainment of microparticles, where the hot melt pool produces an argon flow towards the incoming laser and the surrounding cooler environment.

The produced ejecta presents a problem as the ejected partials re-solidifies and sometimes reincorporated into the melt pool and had been shown to reduce the tensile strength of the produced parts (Liu *et al*., 2015). The usage of high-speed imaging to monitor the AM process had demonstrated effectiveness on validating or observe part quality, although the process was mostly manual and the requirement of a large amount of hardware to process the video data present difficulty in achieving closed-loop feedback.

2.2.2 Thermal Imaging

Infrared system focuses on obtaining electromagnetic radiation with a wavelength of 700nm to 1mm, which uses emissivity data of a given surface to determine temperature estimations and thermal gradients. Schwerdfeger et al. (2012) experimented with near-IR imaging during the EBM process by perform layer snapshots of a post-melt surface and others use it for examining surface temperature information to predict volume experience heat flux due to build geometry, while using it to control material characteristic and part deformation (Paul *et al*., 2014). Correlations between thermographic IR images and build microstructures were made and that by using thermal cycles and results of computational thermodynamic models that calculate the solidification of the microstructures and the kinetics of precipitation, process parameters for EBM system can be guided (Sames *et al*., 2014).

The IR image taken in between layers can be utilized for in-situ control of the machine, as done by Mireles *et al*., (2015) using a FLIR infrared camera proposed by Rodriguez and others (Rodriguez *et al*., 2012). The IR camera measures the radiation emitted from the object as $\varepsilon\tau W_{obj}$, the reflected radiation from ambient sources $(1-\varepsilon)\tau W_{refl}$, and emission from the atmosphere $(1-\tau)W_{atm}$, shown in Figure 2.3. The total received radiation power can be expressed in terms of the total measured camera output voltage U_{tot} (Rodriguez *et al*., 2012).

$$U_{tot} = \varepsilon\tau U_{obj} + (1-\varepsilon)\tau U_{refl} + (1-\tau)U_{atm} \quad (1)$$

Figure 2.6 shows three different sources of energy, W that the IR camera receives translates to a camera output voltage U. The signal U is obtained by multiplying a constant C (by FLIR Systems AB) by the radiation power W (Maldague, 2001) from Equation 1, where ε is the

emissivity of the object and τ is the transmittance of the atmosphere. Mireles *et al*., (2015) developed LabVIEW code to automate the image acquisition and control of the ARCAM software to adjust beam parameters between layers. This study reported success in detecting pre-generated porosities within the build and producing graded microstructure within a single part. Rodriguez *et al*. (2012) also reported emissivity difference between powder and solids, since powder material exhibits a much higher emissivity, which contributes to most of the received reflected sources by the IR camera. The transient temperature decay factor makes the IR measurement differ from the actual temperature, therefore by recording in IR videos, changes between powder and solids can be observed, although the accurate temperature is difficult to resolve using IR alone.

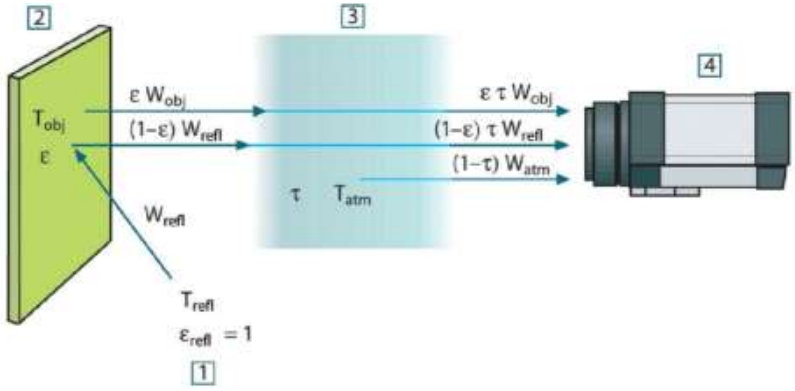

Figure 2.6. A schematic representation of the general thermographic measurement situation. 1: Surroundings, 2: Object, 3: Atmosphere, 4: Camera. Courtesy: FLIR Systems AB. (Pandet *et al*. 2013)

Despite the limitations in accurate temperature acquisition, high-speed thermal imaging had been successful in studies aim to validate simulations on the thermal condition of the AM process. Lee et al. (2018) had successfully demonstrated microstructure control by using different scan strategy, as verified by thermal imaging. The thermographic data of the melt pool was used

as input for the thermal model to target specific thermal gradient (G) and solidification rate (R). Different scan strategies and beam pattern were used to target columnar to equiaxed transitions in IN718, as the heating of the neighboring region effetely lower the G and appropriate spacing between spots increases R. The pattern being tested is the ghost beam strategy which uses a primary beam to perform the melt and a following secondary to reheat the as-formed melt pool. Jamshidinia and Kovacevic (2015) employed a closed-loop monitoring system had been demonstrated capable of detecting heat accumulation due to surface roughness, as these defects can be mitigated with powder dosage control, beam current intensity, and beam scan strategies.

For laser systems is well suited for pyrometer measurement, as the direct contact of the object of interest and the device is not required. The studies done by Pavlov et al. (2010) used a bi-color pyrometer that was integrated into the laser machine's optical scanning system and found that the signal feedback from the pyrometer can be sensible enough for further in-situ control integration. Cordero *et al*. (2017b) demonstrated that pyrometers are capable of obtaining more detailed, localized temperature data from the build platform, and suggesting that while it could be a good substation for thermocouples, it is not as versatile as IR cameras.

Another complicating factor in performing in-situ EBM monitoring using external devices is the requirement of a clear line of sight are subject to metallization of the viewing port caused by evaporation and condensation of metal from the melt pool during the process. To mitigate the situation apparatus such as Kapton films (shown in Figure 2.7.). It would often utilize a motor driven Kapton film roll (Dinwiddie *et al*., 2013) that acts as a sacrificial barrier against metallization. Another solution is to use mirror protected window, where a mirror directs the field-of-view of the IR camera away from the build chamber to avoid a direct line-of-sight of the powder bed (Dinwiddie *et al*., 2013). The scrolling motion of the film is sometimes hampered by

friction and vacuum, which could cause the film to melt under high temperature, plus metallization of the Kapton film changes the transmissivity of the material which reduces the amount of infrared radiation reaching the IR camera, resulting in a lower approximation of the calibrated temperature (Raplee *et al*., 2017)

.

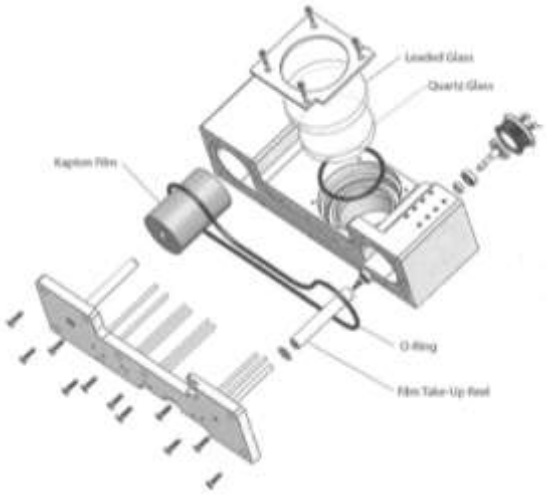

Figure 2.7. Exploded schematic view of the Kapton Film based shutterless window protection system. (Dinwiddie *et al*., 2013)

2.3 Introduction to Electron Imaging

Electron monitoring was first proposed to be a method of tracking the seams between welds in EB welding (Graham and Wingfield, 1965). These researchers envisioned a real time detector that assured the welding beam accurately track the seam of the weld piece. The design was an in-line detector comprised of an isolated metal disk that was symmetrical with the beam port and surrounded by a Faraday shield. It had also proposed to synchronize the electron signal with the deflection coil of the gun in order to construct accurate 2D images of the surface. Wollenhaupt *et al*. (2014) suggested using the scattered electron signal coming beam as a means of monitoring

the condition of the workpiece and give examples of using a simple metal plate to collect all the types of scattered electrons. It also indicates the detection of the secondary and backscattered electron coming from the melt pool is a possible way extract information from the different layers of molten material.

The principle of this type of detection is similar to the gaseous secondary electron detector (GSED) used in environmental scanning electron microscopes (ESEM).Secondary and BSE emissions from the sample complete a biased circuit connected to a metal plate located on top of the chamber, where the detected electron produce current (Knowles and Smith, 1999). The actual condition of the secondary electron (SE) and backscattered electron (BSE) emission inside the EBM system had not been studied until recently, it has been shown that it's possible to take geometric measure of the material and even see the condition of the melt pool (Arnold *et al*., 2018) with electronic imaging, which would be discuses later.

2.3.1 Background on SE/BSE

Electron imaging in general is utilizing an electron source (electron gun) to deposit a stream of electrons (incident beam) to hit the target of interest, as the beam hits the target a plethora of event occurs to generate various signals (shown in Figure 2.8). Secondary electrons (SE) are generated from inelastic scattering of electron s originated from the target material. Scanning electron microscope (SEM) are signals generated from the entrance side, and only at a depth of 0.5nm to 1.5nm where the secondary electrons are generated can escape to surface (Seiler, 1983). SE can also be produced by the BSE and its contribution to the SE yield was investigated by Everhart (1958) and Kanter (1961)]. The SE yield is given by Equation 3 (Goldstein, 2003):

$$\delta = \delta_{PE} + \eta\delta_{BSE} = \delta_{PE}(1 + \beta\eta) \quad (3)$$

δ_{PE} is the number of SE emitted for every primary electron (originate from the incident beam), δ_{BSE} is the number of SE emitted per given BSE, where as $\beta = \delta_{BSE}/\delta_{PE}$. Due to the lower average emergence angle of the BSE, it's more favorable for the excitation of SE than the incident beam itself, β is always > 1, and according to Bronshtein and Dolinin (1968) β decrease as the angle of the incident beam increases.

Backscattered electrons (BSE) are the electrons originated from the sources that got diverted by the atoms inside the target, underwent a series of elastic scattering event.

$$\eta = \frac{I_r}{I_0} \quad (4)$$

Equation 4 describes the BSE coefficient η, and denotes the fraction of backscattered electrons to the incident beam electron (Equation 3), I_r is the current of electrons backscattered into angles > 90 °, and I_0 is the current of the incident electron beam. The η coefficient increases as the target's atomic number increases; hence BSE can be used for compositional imaging (Napchan, 2001). Backscattered electron has a much more angular distribution compare to SE, and are more energetic it easier to detect. As BSE scatters between atoms within the target it will produce SE signals and would add to the total SE yield, and by subtracting the BSE signal it's possible to suppress the less localize material information (Niedrig, 1978).

Transmission electrons are the original electron beam that passes through the target. This, along with the SE generated from the back side of the target, are the signal source for equipment such as transmission electron microscope.

Other species include Auger electrons, characterized by the Auger effect, which are the outer shell electron energized by the vacancy of an inner shell electron, which can be elastically

removed by the incident beam. During these interactions X-rays and cathodoluminescence are emitted from the surfaces a will, the former can be used as energy dispersive X-ray spectroscopy (EDS) and the latter as optical image of the target with color. Electron beam induced current (EBIC) are the electrons originated from the incident beam that was absorbed by the target, it is most commonly used as a way to probe subsurface p-n junctions in semiconductors. (Goldstein, 2003)

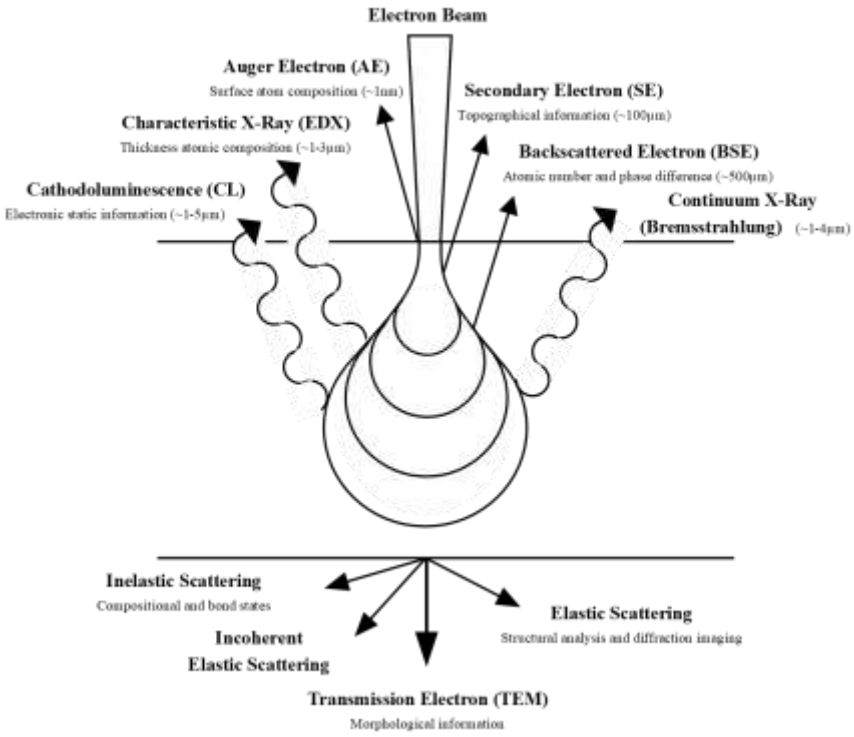

Figure 2.8 Emission of various electrons and electromagnetic waves from the specimen.

2.3.2 Electron Detection Hardware

The most widely used SEM detector is the Everhart-Thornley (ET) detector (Robinson, 1973) that utilizes a photomultiplier to amplify the faint trace of photon given off by the scintillator when it was struck by an electron. A grid of metal mesh covers the tip of the scintillator is biased positively in order to attract low energy electrons such as SE that are distributed below 50 eV,

modified version of ET detectors uses a dynamically bias range from -500V to +500V as the negatively bias mash would repeal electrons at the lower energy level while the higher energy ones like BSE would go through; this type of detector was later dedicated to SE detection as others types were investigated due to its poor resolution (Kimoto and Hashimoto, 1968). Originally, ET detectors were design only to detect SE, however, later modification uses different biased voltage to detect both SE and BSE.

Solid-state detectors or p-n junction detectors are a piece of annular (Wolf and Everhart, 1969) semiconductor and sometimes are divided into four quadrants for directional accuracy, it's useful for some non-imaging applications, for example, these detectors are capable of topographic and compositional contrast (Kimoto *et al*., 1966), or channeling contrast (Coates, 19670. While the annular solid-state detector was widely implemented, the low gain and slow frequency of these detectors generally produce inferior results with a lower SNR (Robinson, 1980) compared with ET type detectors.

Other detectors intend to subsequent detectors aim at better BSE detection by placing it closer to the target and biased it to ground, thus excluding the SE signals (Cordero *et al*, 2017). Wells (1974) experiments with different ET detector placement and found that the takeoff angle produce a better compositional image, whereas a low takeoff angle produces a better topographic image. These findings were experimented in modern detector designs (shown in Figure 2.9). Another type is the converted BSE detector which converts the incoming BSE signal into SE by placing a negatively biased grid placed over the detector to divert the incoming BSE (Reimer and Volbert, 1979), this type of detector is able to produce low SNR image even at low accelerating voltage (Moll *et al*, 1978).

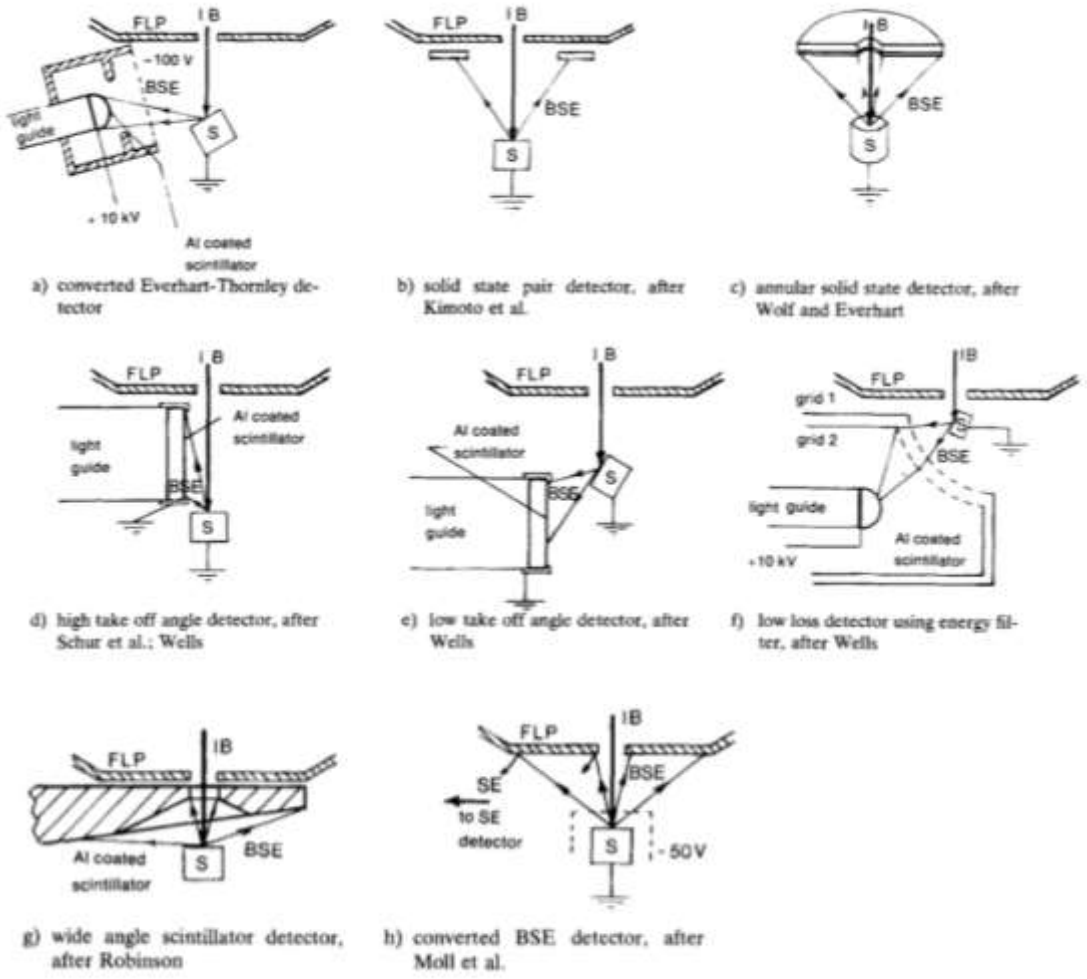

Figure 2.9. Different types and configurations of BSE detectors. (Coates, 1967)

SEM has constrains on the types of specimen it can examine due to its vacuum chamber, however, various technology advancements targeted at organic materials had aim to solve this issue with chambers that can operate at low vacuum pressure. Variable pressure scanning electron microscope (VPSEM) operates at a sample chamber pressure of 2 Torr, whereas environmental scanning electron microscope (ESEM) aimed at a pressure of 50 Tor (Mohan *et al*., 2006). At this level of chamber pressure the mean free path for SE is down to a few μm, reducing the total number of SE reaching the detector; this makes the deployment of ET type detectors not ideal

since it requires the detector parts to be biased to several thousand volts, which has the possibility of flashing over to ground with the presence of low pressure gas. Danilatos (1983) overcame the problem by using the gas within the chamber as a means of amplifying the electron signals, the amplified SE signals are detected by a positively biased metallic ring or wire and then connected to an electronic signal amplifier that's grounded to the machine (Danilatos and Robinson, 1979). This type of detector, also known as GSED, has demonstrated to produce similar quality SE images to that of the ET detectors, this id due to the fact that SE exhibits the highest interaction cross section amount with incident beam and BSE that are also populating the specimen chamber (Farley and Shah, 1991). Danilatos (2012) continues to investigate the alternative of solid-state detectors to abstaining the BS information from a gaseous environment, for it generally has a lower SNR compared with scintillator device due to their detective quantum efficiency under SEM configurations (Baumann and Reimer, 1981), and Oatley (1985)). In this case an yttrium aluminum garnet single crystal as the scintillating device that situated in the same location for solid-state detectors but does not require the bias element in traditional ET type scintillation device to attract the electrons.

2.3.3 Electron Imaging in AM

In metal 3D printing, this electron monitoring technology is first implemented in the EBM system by swapping the original ARCAM S12 gun assembly with an industrial electron beam wielding gun with a build in BSE (Arnold *et al*., 2018). This work is the first to demonstrate in metal 3D printing, the potential of electron imaging technology and its advantages over optical imaging, as the incandescence phenomena of the electron gun is negated (Wysocki *et al*., 2017).

Arnold *et al*. (2018) performed layer images during an extra procedure for each layer, after the melting of the powder, to investigate the porosity detection capability of the system. An article was built with 165, 210, 255 and 300 W to artificially create lack of fusion porosity. Subsequently, the article was X-ray CT scanned to verify the electron imaging result. In comparison with CT images the BSE generated images are limited in terms of its special resolution but had shown promising capability in porosity detection and had suggested using off-axis electron detectors to obtain more information of the surface typology. Using the same setup, the electron images had been used to verify the process window of Ti-6Al-4V (Pobe *et al*., 2019), suggesting it as a tool for future process parameter development.

Wong *et al* (2018 a,b,c) on the other hand, modified the heatshield of an ARCAM A1, using the principle of GSED in ESEM, illustrated in Figure 2.10, where a piece of metal was utilized to pass the small current induced by the received electron to an amplifier, where the output of that signal was being subtracted from the amplified signal of a noise plate, which was another isolated piece of metal plate behind the detector plate. Such arrangement was aimed to increase the SNR and shown to be affective in producing quality image of the target.

To initially test the setup Wong *et al* (2018 a,b,c) performed a low current scan of 1mA and the beam speed of 11800 mm/s was used to generate the scanned image of the standard A1 build plate, and the capability of the systems' performance under high temperature environment

was also investigated. Samples was also heated up to 650°C to observe the detectors performance with different temperature, with the electron beam coordination data obtained from the gun XY deflection coil voltage control, and the intensity of the signals were populated into the corresponding location as grayscale bitmap, and had point out in the author's previous work. The author's subsequent research (Wong *et al*., 2019) concluded that the resolution for the experimental set up is limited to the beam size of the machine, hence a limitation to the magnification of the image. The result of the experiment was examined with histogram-based image quality factor Q, which represented the degree of separation between the two-pixel value classes and found that the elevated temperature had little effect on the quality of the image. This finding on the performance of the experimental imaging device along with the physics of the SE emission, where the kinetic of the atom out weights the effect of temperature (Bruining, 1954), further strengthen the possibility of an in-situ electron base monitoring device in EBM system.

Figure 2.10. Electrically isolated heatshield tested in the early stage of this work.

2.4 Literature Summary

This review covers the current methods of monitoring and forms of data extraction for the building environment of powder bed AM processes used in pass experiments, including the detail of the setup, observed data and some of the results listed in literature. These monitoring methods enables the studies of powder bed machine parameters, conditions of the melt pool created during different processes, and for some experimental setups, the quality of the monitoring method itself. Many of the studies conducted with the outlook of achieving in-situ process monitoring, meaning having a real-time control parameter changes during the machines operation, while in most cases reach the step of validating the monitoring system few complete the step of real-time parameter change mid build.

Each methods of monitoring have the strength of its own and limitations, with optical and thermal systems in general requires optical path the extract data from the build environment it is less challenging in laser systems than in EBM systems. Many of the studies includes the thermal information of the building environment for the fact that the meteorology of the material which closely related to its applications, is dictate by the microstructure formed at different thermal profile of the build environment. Other challenges of in-situ control of the machine with image feedback is the amount of computing power and the time delay for image analysis, for example, the high-speed camera image, or to deduce what parameter to change for certain hot spot detected by inferred camera, and in most commercial solutions it’s difficult to manipulate the control parameters to respond to the required changes software wise.

CHAPTER 3: Electron Monitoring of EBM System

3.1 Introduction

The EBM apparatus of the EBM system allows for the principle of BSE imaging to be implemented as a means of a non-intrusive monitoring method, similar procedure was performed in scanning electron microscopes (SEM) and electron beam welding machines (Wollenhaupt *et al*, 2014). In order to estimate the signal range of any electron event caused by the incident beam Wells (1970) model of electron interaction was considered, where signals from the elastic, inelastic electrons, and the transmitted electrons combines to be the incident beam's intensity. As the capability of layerwise electron monitoring in EBM being experimented by Arnold *et al*. (2018) it has been proven to be an effective way to detect the formation of post melt surface porosity, yet the system implemented in the apparatus was a commercially available electron gun with built-in BSD detector and supporting imaging software (Clauß, 2018); in order to perform electron imaging with the gun system of the ARCAM machine additional data acquisition interface and imaging software are needed, as well as additional scanning procedure performed by the EBM machine. Electron signals originated from the current passing from the detector element to the build platform is being measured by the voltage differential between a shunt resistor that is in series with the detector (Williams, 1984), a current to voltage convertor circuit with the measurement range of 0 to 20mA was choose to encumbers the operating current range of the electron gun. This chapter will outline the process of designing the detector element, as well as discuss the many experiments and hardware iterations that bench mark the capabilities and limitations of this system.

3.2 Electron Signal Detection

To measure the signals off of the detector plate the necessary physics of the nature of the signal must be understand in order to choose the correct hardware for the task. The electron interaction in the EBM system is much more complex than an electron microscope or in EB-welding, as the more energetic interaction of the EBM will create positively charged metallization and plasma that would interact with the incident beam (Klassen, 2017).The phenomenon had been studied in the field of vacuum deposition where the vaporization element would be created by a pulse laser or an electron source. Two solutions to avoid the line-of-sight interaction are the bent-beam and tilt-beam vacuum chamber design, which had be employed in the study of uranium atom beam vapor velocity (Ohba *et al*., 2000). It was found that the electron impact excitation and ionization of the evaporated atoms are proportional to the amount of electron-atom collision and the acceleration voltage of the electron source. As the material surface being further energized by the incoming electrons it was found in the study of uranium charge partial species, that the total thermionic emission would only exceed the combine signal of elastic and inelastic electron interaction at a 2200K surface temperature (Nishio *et al*., 1992), and in the case for copper the temperature would exceed 2500K (Dowell, 2013).

Hence it is concluded that the main contributor to the signal during the scanning as well as melting of the powder surface are electrons generated from the elastic and inelastic interaction of the incident beam. Events such as spatter and target density will yield a change in electron signal intensity, and in the case of smoking events where the charge build up could represent an inverse of current flow, these could, theoretically, yield information concerning the condition of the melt pool.

3.2.1 Theory

The signal generated form all the electron sources form the chamber of the EBM machine can be simplified with the basic theory of electricity. Assuming a vacuum environment in Figure 3.1. (a), the discharge (+) e supplied with v from point A move a distance of ds in an electric field E, transferring a charge of dq from electro tip A to B under the potential of V under a time of dt. The current i is dq/dt, or:

$$i = e\,E * v/V. \tag{6}$$

The same charge calculated in equation (6) can be connected even if the electrodes are not connected, or connected through a very large resistor as in Figure 3.1. (b). The electrodes will be connected through a resistor R and shunted by a resistor C equal to the distributed capacitance of the system. The mode of charge flow through the system is determine by the time constant RC, which would output a differential voltage signal Vs across the resistor. A simplified schematic of the ESEM (or EBM) machine's electron gun shown in Figure 3.1. (c) illustrated a negatively biased gun anode at point G at $-V_b$, referenced at the cathode point A, upon discharge a beam of electron to hit the target of interest C which would have induced a current to flow from the target to E the chamber wall, F the electron detector plate, or D the base of the specimen, in multiple forms of electrons.

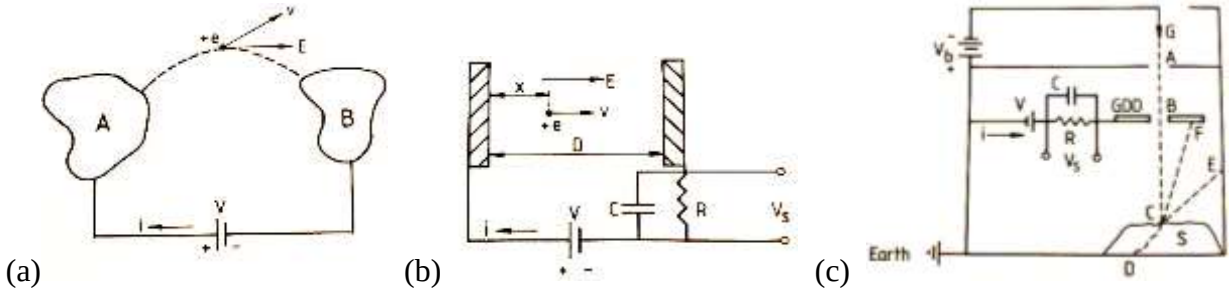

Figure 3.1. (a)General-shape conductor, (b) Parallel plates, (c) Simplified ESEM

The amount of current carried by all the interacted electrons would fallow Kirchhoff's circuit laws, in which case the current passing through the secondary electron and backscattered electron i_{SE} and i_{BSE}, along with the absorbed specimen current i_{SC} would add up to equal the incident beam current i_B, shown as:

$$i_{SC} = i_B - i_{BSE} - i_{SE}. \quad (7)$$

The backscatter electron current will be $i_{BSE} = \eta\ i_B$ and the secondary electron current will be $i_{SE} = \delta\ i_B$ (Wells, 1974), which would give us a range of what the electron signals inside the EBM machine would look like. This analogy gives us a clear range of what equipment is best suited for the current measurement, depended on the different backscattered and secondary yield of the target material the signal produced inside an EBM will be in the range of 10 µA to 100 µA in reference with the ground of the incident beam. Under the vacuumed environment of ARCAM A2 with the preheat current of 25 mA, material such as copper would have a theoretical yield of 0.34. Reports of the backscattered coefficient and the secondary yield that exclude the contribution of backscattered-induced secondary are found to be 0.25 and 0.1 for an acceleration voltage of 60 keV.

3.2.2 Monte Carlo simulation

To understand the condition of the how the beam interacts with the target area interaction volume simulation software CASINO v2 is used to determine the take-off angle and the information depth of the apparatus (shown in Figure 3.2), the former is used for efficient detector placement whereas the latter can indicate the information depth of the resulting signal. The program utilizes the Monte Carlo method to estimate the possible pathways where electrons can travel within solid materials, with the initial sets of boundaries defines the domain of possible inputs, the results will be derive from the aggregated possible probabilities through deterministic computation on the inputs (Kawrakow, 2000). Initial conditions of the program use the copper plate with a thickness of 20mm, and the properties of the beam includes a 60kV acceleration voltage as well as a 200µm beam diameter. The result indicates a detector placement that covers 0 to 55 degrees (referencing the incoming beam) would be optimal for capturing the BSE signal which conforms to literature data (Reimer and Riepenhausen, 1985), whereas the trajectory of SE is highly dependent on the incident beam angle; with the operation range for the EBM system the SE to have a high take-off angle of 30 degrees at low acceleration voltage, while converging toward 60 degrees at high acceleration voltage (Carriere, 2018).

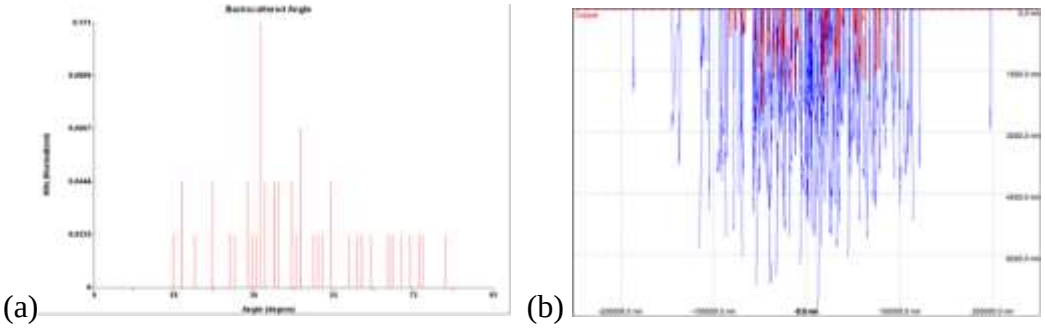

Figure 3.2. Casino simulation on (a) angular distribution of the exiting BSE and (b) interaction volume

3.3 Experimental Setup

3.3.1 Hardware Design and Iteration

The hardware setup, shown in Figure 3.3, for collecting the electron induced current signals within an EBM machine was inspired by the design and research done by Wong *et al*. (2018) and Arnold *et al* (2018). For the initial validation of the image collecting capability of the detector a heatshield of the ARCAM A2 was electrically isolated with alumina oxide ceramic material, connected to a transimpedance amplifier to convert into a voltage potential for the data acquisition device for logging. Data for determining the precise location of where the beam was as well as beam current, was obtained by tabbing into the machines control PLC. Scans of the surface of the build was performed on the A2 custom small build tank while building with OFE copper; it was happen to be what the modified machine was experimenting on at the time of the experiment, but also happened to have the added benefit of a lower melting temperature compared with Ti-6Al-V4 or other experimental material, provided a less harsh environment for the experiment, as well as having a high conductive metallization on the heatshield detector that would still enables the passage of the current signal.

Figure 3.3. Detector hardware iteration

3.3.2 Automatic Data Acquisition

The electron gun used in the ARCAM A2 is Rogowski-type tungsten filament electron gun that uses the thermionic emission property of the material to generate the streams of electrons. As the electrons exit the filament, they are being regulated by the biased electrode using the space-charge limited regime (Carriere, 2018). This takes the control of beam current away from the temperature-limited regime of the thermionic device, which can provide a faster respond time in changing the beam current. The control bias voltage to the biased electrode, or grid cup, has a feedback PLC voltage signal, which shows a polynomial trend with respect to the commanded beam current from 0.1 mA to 20mA.

$$V_{grid} = -0.1741 I_b + 6.426 \quad (7)$$

As V_{grid} is the grid cup control voltage and I_b is the corresponding beam current output. This has the potential for giving feedback to the electron imaging and control system, and at later stage of the development it has been used as a triggering signal for the auto logging user interface. In order to obtain the coordinates of each data point, what is essentially needed is where the beam is pointing at in a given moment. The electron gun uses a series of magnetic coil to focus and reshape the stream of electron, called condenser lenses, whose physics works in a similar fashion as optical lances (Goldstain, 2003). Underneath the condenser lenses are the deflection coils with dipole magnets who's a magnetic field tangent to the beam to push the beam on two axes, with the trajectory is change according to Equation (8):

$$\sin(\theta) = 2.97 * 10^5 \frac{l * B}{\sqrt{V_{cc}}} \quad (8)$$

As *l* is the length of the field and B is the magnetic field strength. The strength of the field can be change according to Ampere's Law by the loops of winding current-carrying wires, define by Equation (9):

$$\mathrm{B} = \mu_0 \frac{N * I_a}{S} \tag{9}$$

Where $\mu_0$the permeability of free space, N is is the number of coils, I_a is the current waveform created by the signal amplifier and S is the pole piece spacing. As l is significantly larger than the distance from the center of the deflection system to the target, the distance for which the beam would travel due to the change in field would be tangent to the center axis of the beam. If assuming a small change in angle, as $\sin(\theta) \approx \tan(\theta)$, in this case equation (8) and (9) can be combined to yield a beam velocity of:

$$\mathrm{v} = \frac{dx}{dy} = 2.97 * 10^5 \mu_0 \frac{N * l * z_{def}}{\sqrt{V_{cc}} S} * \frac{dB}{dI_a} \frac{dI_a}{dt} \tag{10}$$

This shows that a deflection angle of less than 15 degrees would have a constant beam velocity, exceeding it would require a fast, dynamic focusing system to offset the non-linear acceleration at high deflection angles. With the working distance of 330mm and build surface of 200 x 200 mm in the standard build tank, and the build surface of 40 x 40 π mm for the small build tank setup this effect can be omitted. The deflecting system has a mathematical model with a stationary and a dynamic part. Stationary model is a particular solution of the dynamic equations of the electrons when the electric and magnetic field distribution is known (Oltean and Abrudean, 2008). The relation between the deflection distance on a linear axis and the deflection current is:

$$x_{defl} \approx \sqrt{\frac{e_0}{2*m_e}} * \frac{K_b*\mu_0*d_{defl}*l_b}{a*\sqrt{U_{acc}}} * n * i_{xdefl} \quad (11)$$

d_{defl} is the distance from the coil to the material surface, l_b the coil length and a is the coil dispersion constant. The dynamic model of the deflecting system on the linear axis is given by:

$$L_s \frac{di_{xdefl}}{dt} + R_s i_{xdefl}(t) = u_{xdefl}(t) \quad (12)$$

The control system of the ARCAM uses PLC signal to control the deflection hardware, which is also outputs a linear signal to the deflection coils current input controller. Preliminary experiment on the PLC signal output shows a linear relationship between the previously mentioned control signals and the distance traveled on the build plate, showing a possibility of using it as a coordinate system for the graphical representation of the electron signals. During the hardware developing stage both the PLC control signal and the deflection card control signal had been experimented with and as the resulted image shown in Figure 3.6. The former is clearly the superior option in terms of spatial resolution. Noted that the location of individual pixels is resulted from the interpolation of the signals from the control side, events such as beam defocus due to charge build-up of the surface in a smoke event, beam deflection oscillation due to the instability of the deflection system's power supply (Trushnikov, 2013), or external magnetic field interference.

In order to test the capability of electron monitoring during melt a series of experiments were set up to coordinate the BSE and SE intensity to the melt pool condition. The data collected form the melt pool is closely related to the incident beam current, while other factors could also contribute to the change in intensity of the combined BSE and SE signal. To identify possible correlations between melt pool size with the electron signal intensity two sets of melt tracks with

different parameters was performed, with the first being tracks raging from 3mA to 20mA beam current with the same beam speed, and the second being tracks with a matching PV of 1000 in the same current range.

Process monitoring was also performed during the production of copper cavities for x-band radar applications, for the build duration of 8 hours the automatic logging LabVIEW software was implied to distinguish the start of the preheat period and the end of the melting stage from the amount of the voltage going in the grid cup control. Details of the LabVIEW code can be found in Appendix A.

(a)  (b) 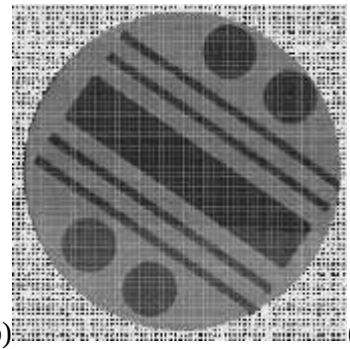 (c) 

Figure 3.4. (a) Image generated with deflection card control signal, (b) Image generated with PLC control signal, (c) Top view of the STL file

With two detector plate placed in line of the incident beam the signals from each cam be combine or subtracted to create compositional or topographical image of the surface (shown in Figure 3.5). The last iteration of the detector design comprised of copper signal plates mounted on a copper ring block, all components are electrically isolated from each other. In compositional mode, signals from the two plate are joined by a BNC interface and fed to the current to voltage convertor, and passed to an X1 gain differential amplifier to subtract from the noise signals originated from the copper ring block. In topographic mode the signals from the two plates are subtracted from each other by a differential amplifier without the input from the noise plate, as any inherent noise signal will be cancel out during the operation. The following experiments are conducted with topographic mode intended to capture any potential melt pool characteristics at a higher SNR, and for the operation range of the beam current a 1KΩ shunt resistor was used for the current sensing circuit.

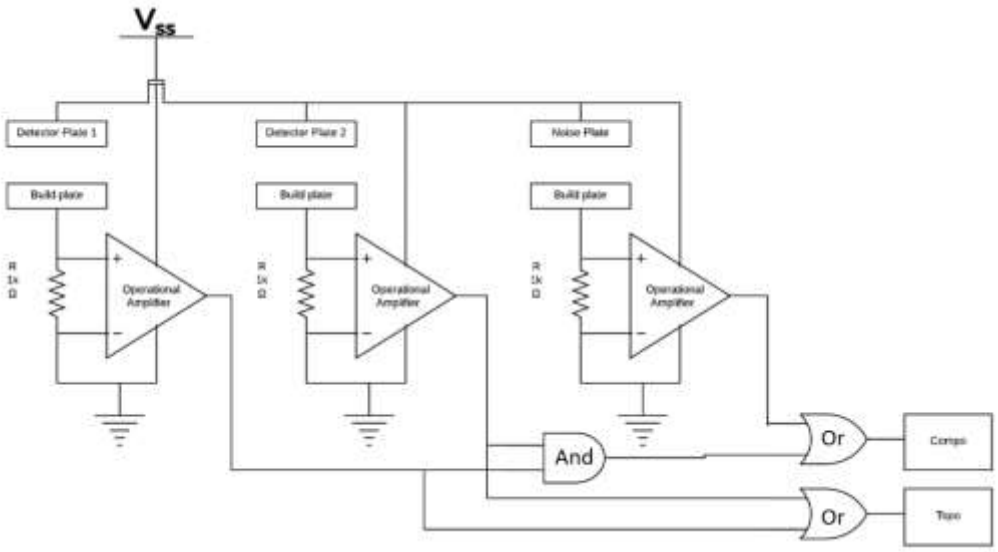

Figure 3.5. Simplified schematics of the amplifier component

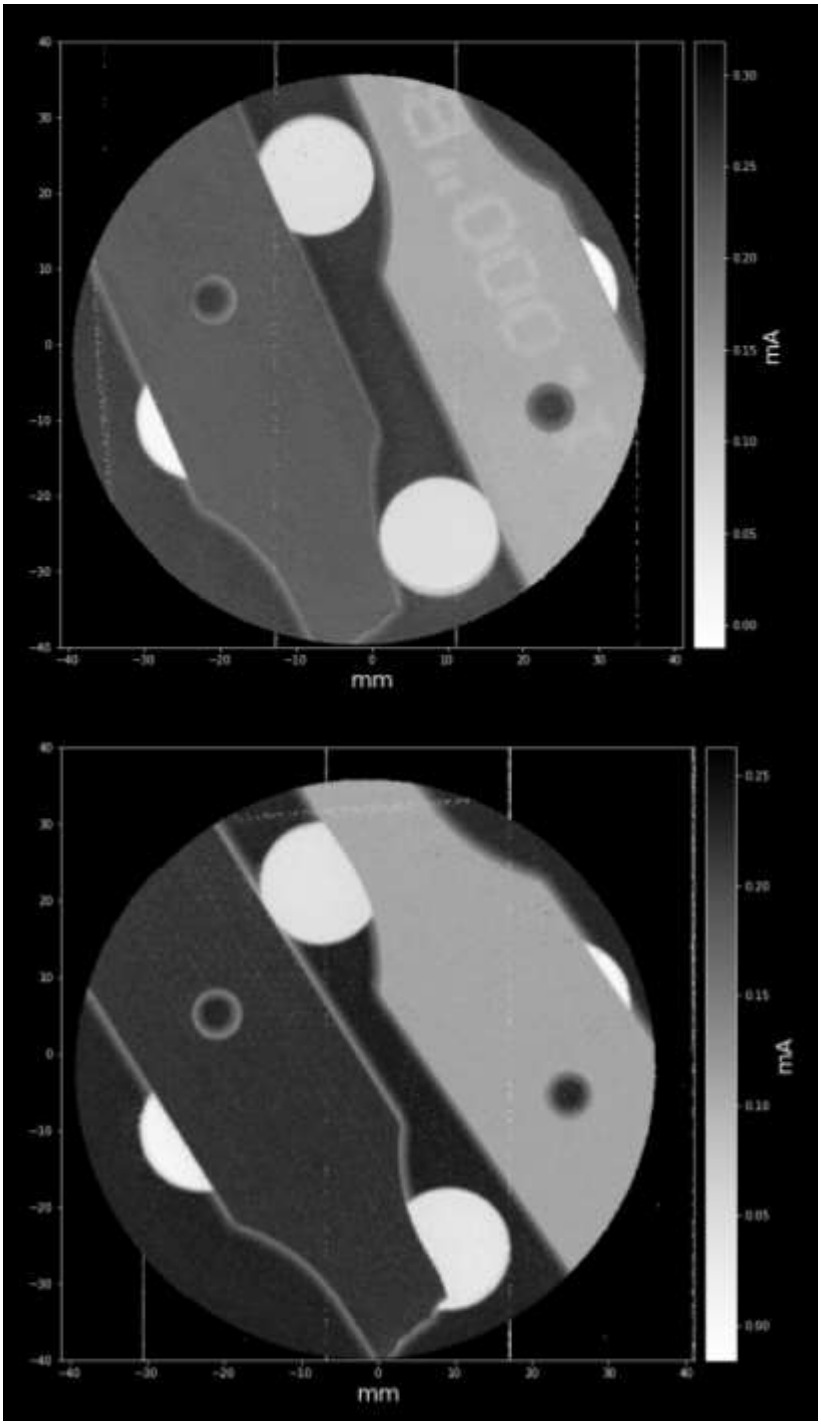

Figure 3.6. Compositional (Top) and Topographic (Bottom) electron image

3.4 Result and Discussion

3.4.1 Melt Pool Characteristics form the BSE Signal

Figure 3.7 shows the comparison in electron signal intensity in the range of 17mA to 20mA, of varying speed to maintain constant PV, and constant speed. While the different melt pool formation did not reflect on the intensity of the current received by the detector, constant speed of the beam represents higher energy input to the surface of the material did create a greater amount of spatter, which give off 25% more noise compared with a constant PV beam.

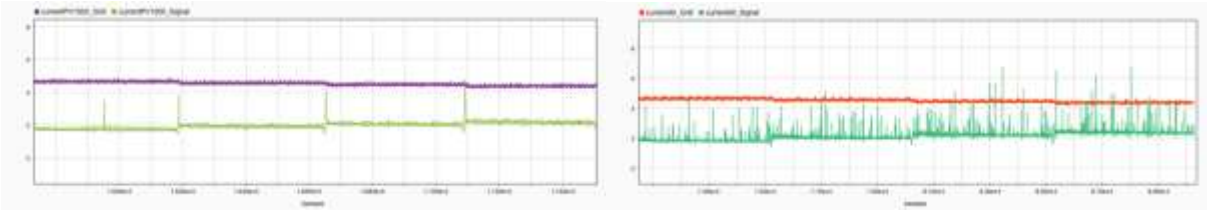

Figure 3.7. (a) Current 3mA to 20mA, constant PV of 1000. (b) Constant speed.

The current imaging technique is unable to distinguish the different size of the melt pool do to the correlation between deflection coil data and the electron signal, for each signal point represents a combination of any point of contact to the part surface and the incident beam's skirt radius of 382 µm (Wong *et al*., 2019), and each interaction event would occur between the surface to depth of the backscattered electron escape volume of around 6 µm. Since the resolution of each signal point around 300 µm, other melt strategies and signal analysis methods are needed in order to deduce the origin of the noise signal.

3.4.2 EBM Build Monitoring

Figure 3.8 (a) shows the current intensity of the electron signal during the melting of a layer. The pattern shown on the surface is theorized to be the melt direction of the previous layer, and with a line offset of 0.13 mm the beam is calculated to have remelted 50 % of the previously formed melt track. A post melt layer scan using a beam current of 1 mA, a beam speed of 10000 mm/s and a line offset of 0.1 mm, reveals a surface roughness condition after the melting process, where the lower intensity region of the melted edge indicates curling. This scan also confirms that the lower density powder layer would yield a lower signal intensity, which would be useful in detecting spreadability issue, shown in Figure 3.8 (c). This procedure would take multiple scan to be able to collect the amount of data needed to construct an image, and for the current parameter set it would take an extra 20 second.

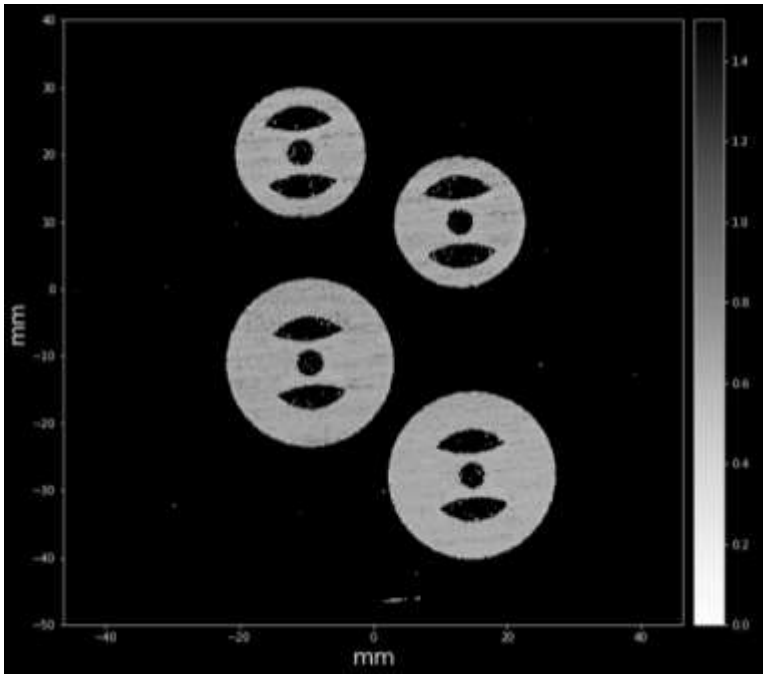

Figure 3.8. (a) Melt pool imaging.

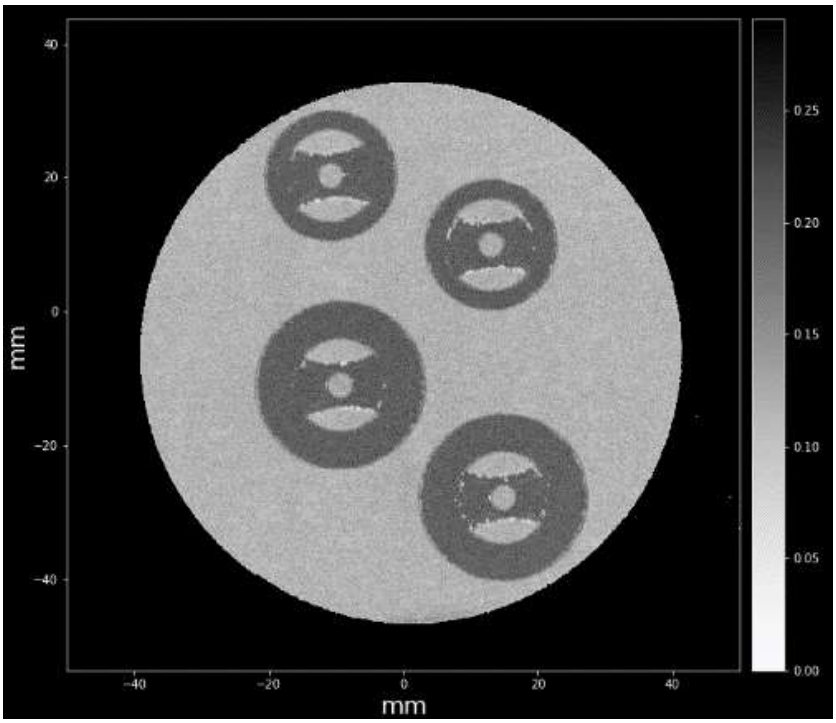

Figure 3.8. (b) A surface scan after a melt is completed

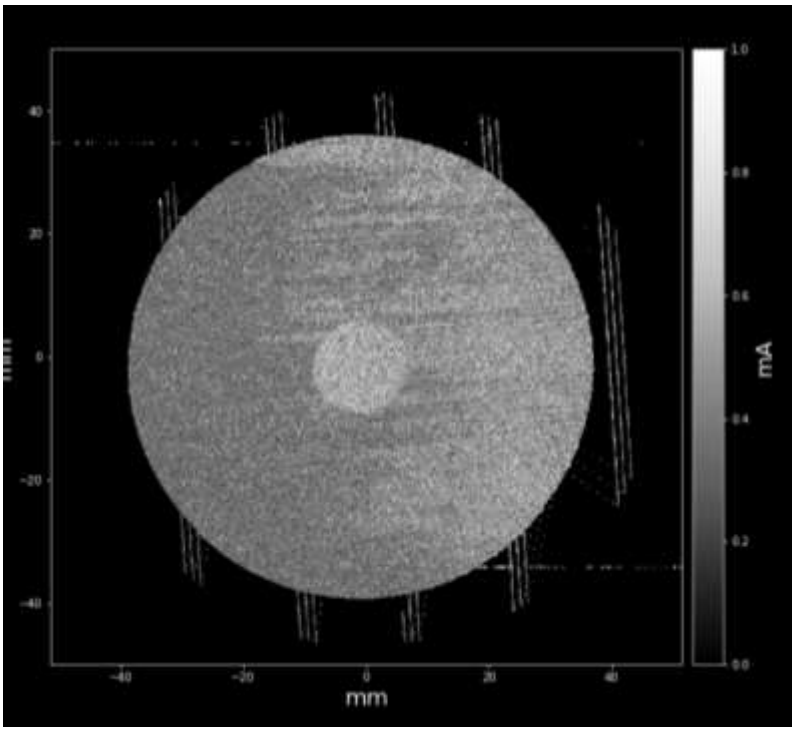

Figure 3.8. (c) Post-melt layer scan

Figure 3.9 shows a stacked rendering of 271 continuous layers. Image processing was performed in ImageJ, using the image stack functionality with interpolation. The cross section reveals the porous overhang region caused by the increase in beam velocity, as well as lack of fusion which shows up as dark spots within the cavity structure. Space within the inner cavities were also rendered with grayscale color due noise signals accumulated during the acceleration of the beam, thus it this should not be perceive as an indication of the density difference between the solid part and the powder bed.

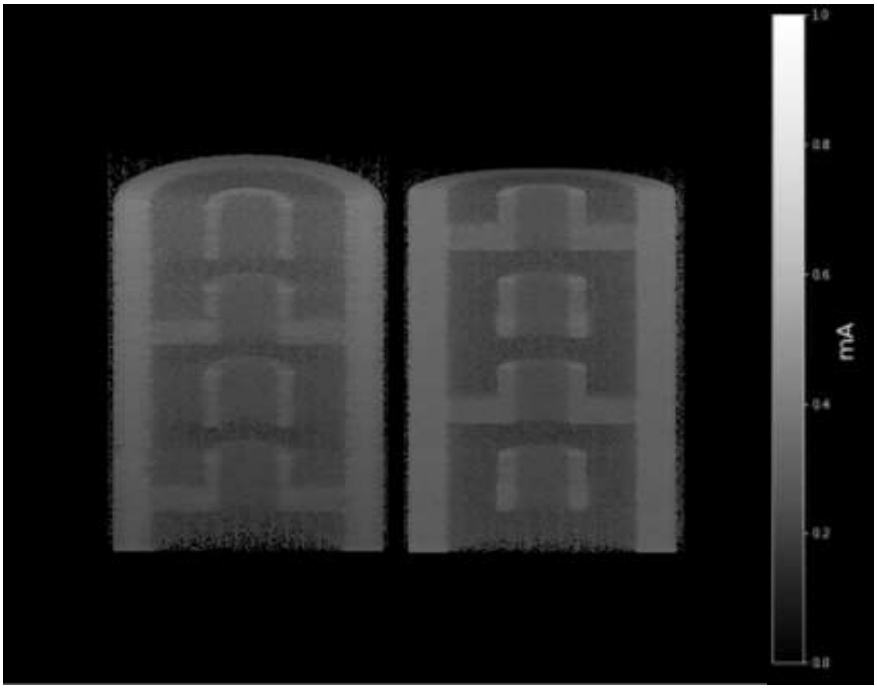

Figure 3.9. Stacked image of 271x 40 μm thick layer

3.4.3 In-situ Melt pool Characterization

Figure 3.10 (a) shows the topographic surface of the melted powder layer in terms of electron signal intensities, which was created through mesh generation of neighboring electron intensities as the z height of the 3D surfaces. The topographical features captures by the electron interaction produces significant contrast in the processed image, which can be conform by micro CT and confocal optical images (Figure 3.10 (b) and Figure 3.10 (c)). The electron signal dropped at locations where gas pockets are formed, as shown in Figure 3.11. This structure was observed with high-speed camera, to originate from the out gassing of water vapor formed from electron beam impact. As the vapor explosive escape the as formed melt pool front it would expand both upward and downwards, where the former was captures as an outburst of material and the latter expanded into the powder bed to form the pocket. With the melt pool front formed ahead of the point of beam, such pocket geometry would also trap the scattered electrons and prevent them from reaching the detector, hence the drop of overall signal. After the beam passes the as formed pocket molten material would colipase and sometimes covered the pocket surface, much like the formation of keyhole porosity.

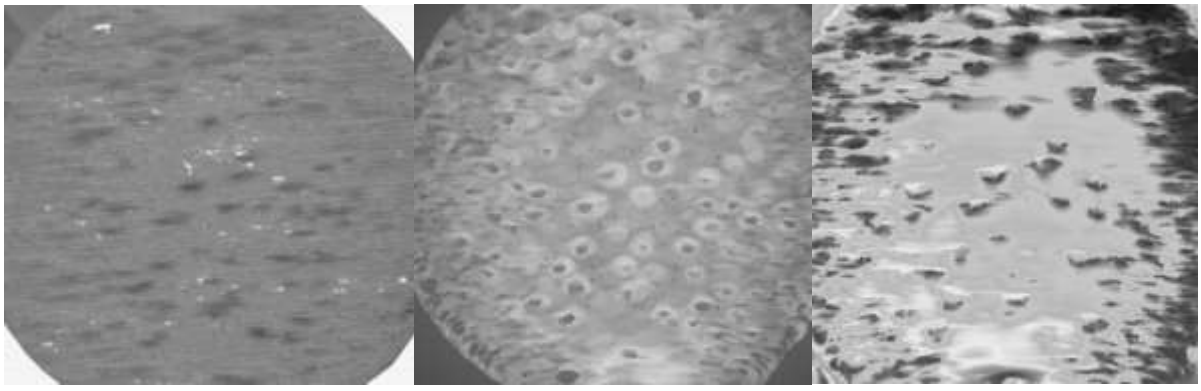

Figure 3.10. (a) Electron image generated during melt, (b) Micro CT image of the surface (c) Image by the Keyence Confocal Laser Scanning Microscope

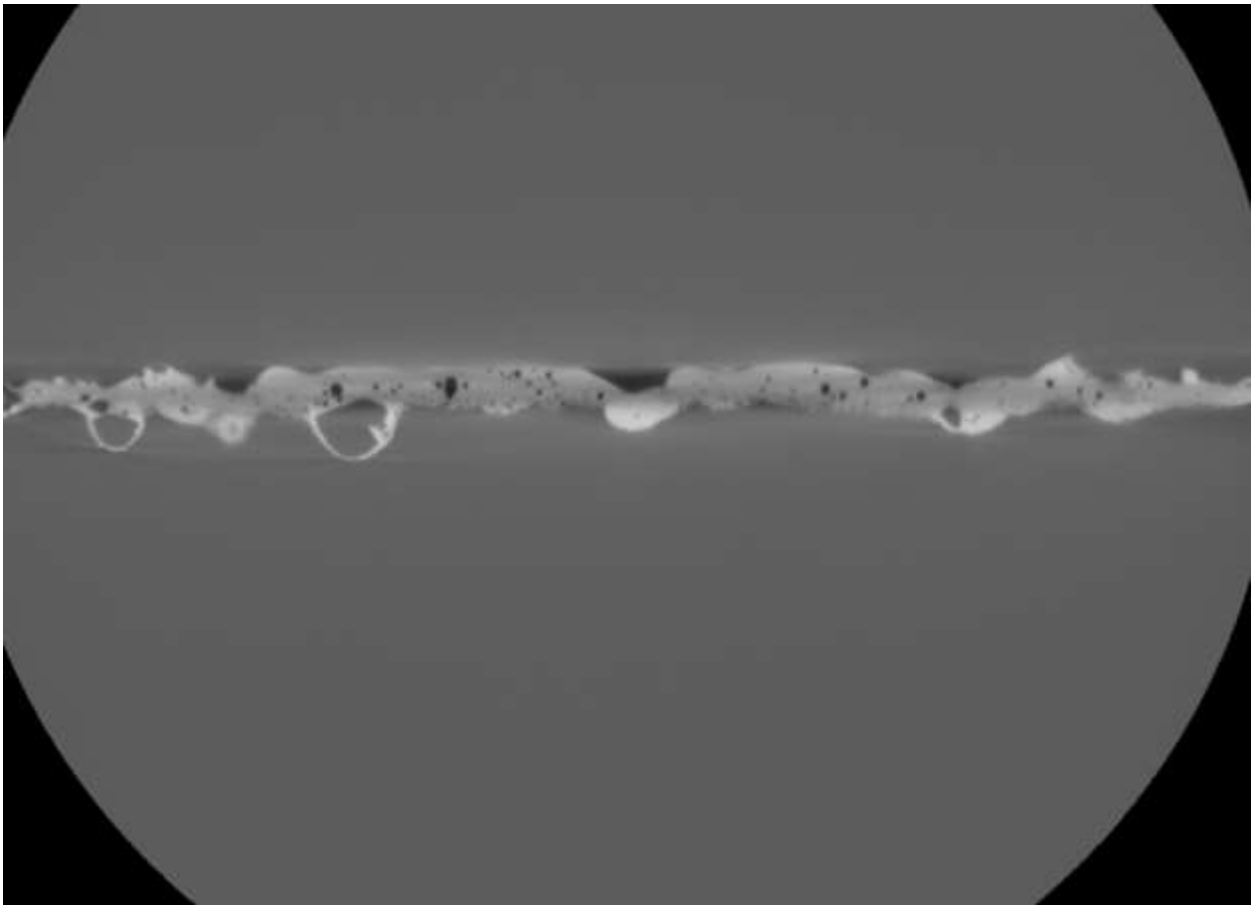

Figure 3.11. Cross section of the CT scanned wafer sample.

3.5 Conclusion

With the introduction of electron optics, comes with an entire new way of studying the melt pool condition of the EBM system. Signals from melt pool created from a higher power input create spatters that reflects in higher SNR, this would theoretically happened if the incoming beam encounters the powder material before it reaches the build plate. In this case the single ejecta would be electrically isolated with the rest of the machine and during the interaction of an incident electron, where the only path to neutral for the BSE or SE created during the process is the detector plate. The extend of the exact ratio of the current that can be conducted through this method although cannot be determine through the current experimental setup, should not exceed the backscattered coefficient of the material multiplies the sensitivity of the detector. During the melting stage of a build the spatter of material is less violent as the 40μm layer would sometimes only contain a signal layer of powder, hence the capability of sublayer porosity sensing ability over thick powder layer would not be applicable on a production build.

On the other hand, smoking events were also observed during the experiment and after examining the electron signals it was discovered that during the suspected even time frame three consecutive instances of negative current flow occurred after a quick buildup of charge, meaning a current passing from ground to the detector. The inverse of current flow is the result from the buildup and subsequent release of charge in the powder bed, and as describe in the study done by Cordero (2017) that it can be treated as a capacitor. With the grounded detector system it can only be speculate that at the point of the electron repulsion occurred on the individual powder partials electric charge is also being carried away from the plate, into the surrounding chamber environment before settling back to the machine’s inner surfaces.

CHAPTER 4: In-Situ Scanning Electron and Process Data Monitoring in the Electron Beam Melting Process

1. Introduction

Electron layer monitoring of the EBM process had become the focus of a good deal of research recently due to advantages compared with optical monitoring methods, such as the lack of incandescence influences occurred in near infrared optics due to the nature of the hardware (Wong et al., 2018a,b [1] [2]). The electron gun of the EBM system allows for the principle of electron imaging to be implemented as a means of a non-intrusive monitoring method, similar procedure was performed in scanning electron microscopes (SEM) and electron beam welding machines (Wollenhaupt *et al*, 2014 [3]). Using the difference backscattered coefficient and secondary yield created by the seams of the weld piece, electron monitoring had been implemented in the feeding back control system of the EB welding process as a seam detection system. As the capability of layerwise electron monitoring in EBM being experimented by Arnold *et al*. (2018) [4] and Pobel et al. (2019) [5], using a commercially available electron gun (manufactured by pro-beam) with built- in BSD detector integrated into an ARCAM A2 machine. It has been proven to be an effective way to detect the formation of post melt surface porosity, yet requires additional scanning procedure performed by the EBM machine. Wong *et al.* (2018 b) [2], on the other hand, electrically isolated the heat shield element within the build chamber and turning it into a detector. The modified heat shield technique requires the minimal amount of modification to the original EBM machine, and has been tested for using a beam current of 1mA and the beam speed of 11800mm/s to generate a surface scan image ranging from room temperature to the 650C (Wong et al., 2019 a) [6], and has been tested to have a z height resolution of 0.35 mm (Wong *et al.* 2019b) [7].

While Arnold and Pobel didn't disclose the details of their image construction technique,

Wong had used the deflection coil signals for acquiring the stepping frequency of the plate scan rastering procedure to transform the electron signals into a 2D image. This research proposes the use of the XY deflection coil signals, not as a reference to process the electron signals, but simultaneously sampled and transformed into spatial coordinates. This allows us to perform electron imaging not as a separate step but instead during the EBMs melting process, and on top of that, mapped other machine feedback control signals as well as details of the electron beam parameters such as beam power and velocity, to the deflection coil data. This monitoring methodology enables the spatial-temporal mapping of any available machine information, internal or external, and providing new techniques for material parameters' development as well as future in-situ process control capability.

2. Methods

2.1. Data Acquisition setup

2.1.1. DAQ Hardware

Sample fabrication and electron imaging were performed on customized ARCAM A2 EBM (V3.2 SP2) and S12 machine which has been modified with a smaller build area and powder deposition system, neither of which are anticipated to adversely influence the results of this study, as shown in Fi g 1. The build chamber was modified to include several view ports providing line of sight to the top of the building platform. Fig1 also illustrates the modifications to the original tank setup. A small, shaft-driven feeder tank (a) and a build tank of equal diameter (b) replaces the powder hopper and the build tank. The shown build tank contains the electron imaging setup, which comprises a left and right detector plate (g,f), a noise plate (e), and an adaptor plate (h). The electron detector plates were made from 3mm thick copper sheet, while electrically isolated from the build tank with alumina ceramic bolts and washers.

Data acquisition was performed by a National Instruments C series 7223 voltage input module, capable of simultaneously sampling four channel inputs at a maximum rate of 500 kHz and providing a 60 volt channel-to-channel isolation. The SEE signal, X and Y deflection coil feedback voltage, and grid cup control feedback voltage were all simultaneously sampled at a rate of 100 kHz. To trigger the automated data acquisition process, a National Instruments 6009 voltage input module was used to acquire the grid cup control voltage at a rate of 100 Hz. Once the grid control feedback voltage reached a preset limit, the high speed data acquisition was only then initiated.

Feed stock powder used in this experiment were high purity copper supplied by Praxair in the as atomized condition. The measured PSD before the EBM process was 89µm for copper, measured by laser diffraction using a Microtrac S5300. An oxygen and hydrogen content of 300ppm and 30

ppm wt., measured by inert gas fusion analysis, using a LECO OH836.

2.1.2. Electronics Schematics

In order to detect the current carried by then secondary and backscattered electrons impacting the detector plates a current to voltage converter is connected in series with the lead from the isolated plate and to ground. The converter measures the voltage across a 1 k Ωshunt resistor that connects the detector plate to ground, providing a milliamp level measurement range. With two detector plate placed in line of the incident beam the signals from each cam be combined or subtracted to create compositional or topographical image of the surface (shown in Figure 2). The last iteration of the detector design comprised of copper signal plates mounted on a copper ring block, all components are electrically isolated from each other. In compositional mode, signals from the two plate are joined by a BNC interface and fed to the current to voltage converter, and passed to an X1 gain differential amplifier to subtract from the noise signals originated from the copper ring block. In topographic mode the signals from the two plates are subtracted from each other by a differential amplifier without the input from the noise plate, as any inherent noise signal will be canceled out during the operation. Comparison of these two modes of layer scan can be found in Appendix C.

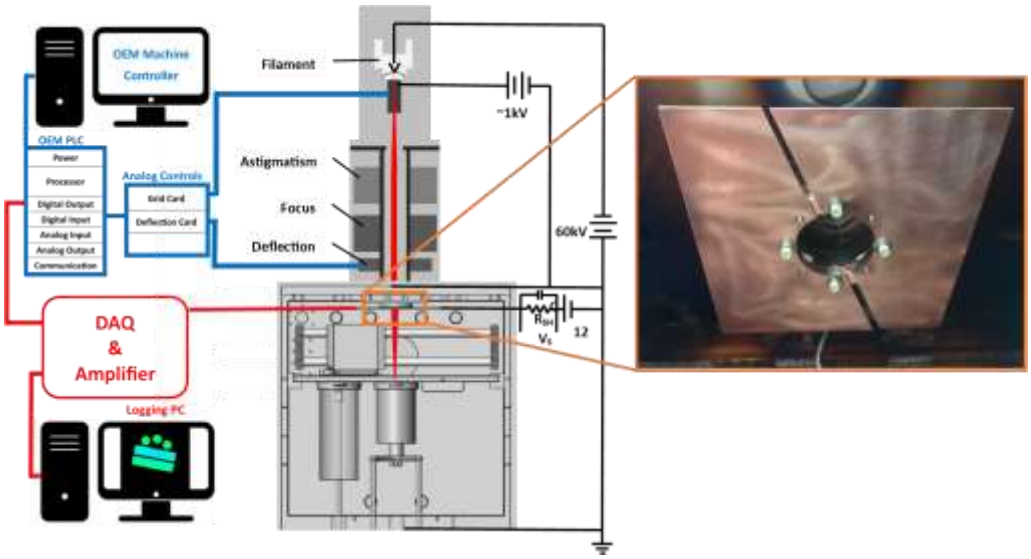

Figure 1: Schematics of the electron detection system and the CAD model of the detector inside the modified build tank. a. Feeder tank, b. Build tank, c. Powder collector bin, d. Rake, e. Detector noise plate, f. Right detector plate, g. Left detector plate, h. Mounting plate for the detector

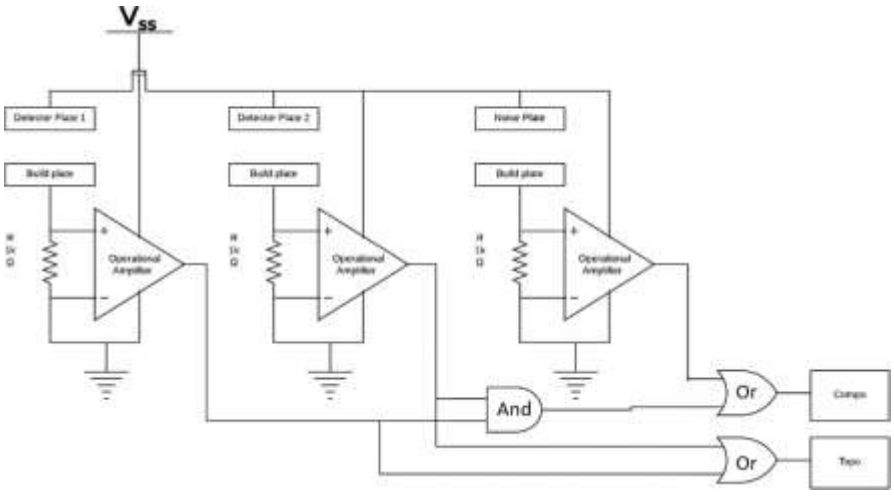

Figure 2: Schematics of the Current to Voltage converter and imaging mode selection

2.2. Image Generation

MATLAB was used to construct post processed images of beam speed, beam current and SEY signal, as a function of location for each layer. Data points are allocated into a set number of bins depending on the image size and then each bin of data was averaged, while the total number of bins for one frame of melt image is chosen for the amount of overlap in the direction parallel to the rastering pattern, shown in Fig 3 (a). Unlike the post melt layer scan procedure, which can use any hatch overlay suited for the task, the beam path during the melt is dynamic and process specific. Hatch length used for the copper DOE build is 130 µm, which is around 50% overlap with a 250 µm beam spot size; this gives us a minimal bin size and pixel resolution of 100 µm, below that would resulted in empty pixels forming strikes parallel to the rastering pattern. Fig 3 (b) describe the optimal bin size with respect to the line offset used during a build, under varying size of beam spots. This relationship of percentage overlap and bin size describes the image resolution in the direction in parallel to the beam path, while the resolution perpendicular to the beam path is highly dependent on the beam velocity and DAQ frequency. Fig 3 (c) illustrates the percentage overlap of beam spots with respect to the range of beam velocity capable of being imaged during melt without under sampling, under varying DAQ frequency conditions. Using the percentage overlap acquired from the previous parameter sets, 50% overlap, as the minimal threshold of image resolution, and combined with the 60 kHz DAQ frequency, we can resolve melt images performed with a raster beam velocity of 8000 mm/s. Melt imaging performed with a higher beam velocity using the same hardware setting would result in under sampled scan lines, this can be mitigate by using a higher DAQ frequency, at the risk of over sampling the PLC XY coil signals which introduce noise in the beam coordinates.

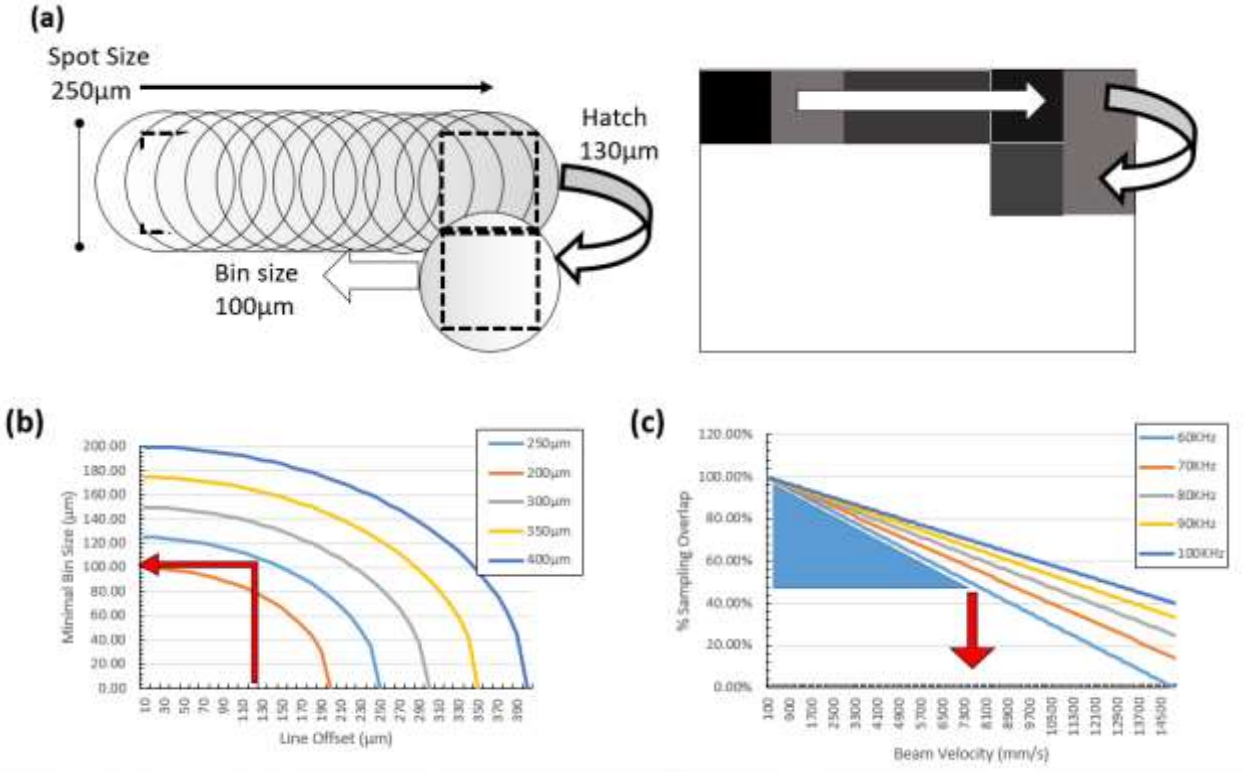

Figure 3: (a) Illustration of the image generation process (b) Bin size and line offset relationship at 50% sampling overlap at various beam spot size, (c) Desired sampling overlap and corresponding beam velocity at various sampling frequency.

During the development of the melt imaging capability it was found that there's a need for acquiring the beam current output due to the nature of the secondary and backscattered electrons. Both elastic and inelastic interaction between the primary beam and the material surface are proportional to the primary beams' current, which are the backscattered coefficient I_{BSE} and the secondary yield I_{SE} respectively. Since the detector setup for this experiment cannot differentiate the two energy sources the image constructed from electron detectors will be a combination of both, which can be quantified in the terms of secondary electron emission (SEE), the secondary electron yield d

(SEY) when for the combined backscattered coefficient and the secondary yield, described in Equation 1, where I_{PE} is the current of the incident beam.

$$\delta = \frac{I_{SE}+I_{BSE}}{I_{PE}} = 1 - \frac{I_{Sample}}{I_{PE}} \quad (1)$$

Research aimed to reduce the SEE in applications such as accelerator and satellite microwave components had drown the relationship between low SEE level and the porosity of the structures' surface (Ye *et al*, 2013) [8]. The effect of porosity count and the aspect ratio of the pores are compared, where the maximum SEY is found to be linearly related to porosity but non- linearly to the aspect ratio while both would react positively in SEE suppression. With possible varying beam current output during the melting process, all electron data points are normalized with its corresponding current output, making image contrasts reflected more prominently by the composition of the material and the topography of the melt pool.

2.3. EBM Beam Control Functions

This study encumbers several designs of experiment build (DOE), performing the materials parameter development of high purity copper and niobium. Most of the experiments consisted of 9 blocks of build material using incrementing mix of two different test parameters. Unlike most LPBF processes, the EB PBF process parameters are determined a priori by a thermal model with two objectives, to maintain a constant surface temperature as well as a constant melt pool size as a function of part geometry and build height. The software calculates the thermal inputs necessary to maintain a constant surface temperature for each layer for the parameters that govern preheating the powder bed, melting the contours of the geometry in a layer and then melting the hatch, or inside of

the part. Using this information, a beam current is calculated. Then for a given current, a beam velocity is selected to maintain a constant melt pool geometry throughout a part. This (speed function) is based on Rosenthal's analytical solution for heat flow with a moving source. Higher order functions accelerate the beam as it reverses direction during rastering to maintain a constant melt pool (turning points function), or to accelerate the beam as it passes over an overhanging feature to account for the sudden change in thermal conductivity between the solid copper bed and the powder (thickness function).

3. Results

3.1. Electron Imaging

Fig 4 shows the comparison between a post-melt layer scan and a melt imaging results. Both data sets were collected during a separate set of copper DOE build. Six complete scans of the surface using a circular geometry encompassing the entire build plate was performed after the melting process was completed during each layer, using the beam parameter specified on the top left of Fig 8. Both images are taken with the topographical mode of the setup to maximize the contrast created by surface pores. The post-melt scan images in theory are higher in terms of topographical resolution compared with the melt images, yet the lower SNR due to less current input during the scan procedure manifest as a lower feature contrast on the topography of the surface. The contrast of the melt images is influence heavily by the aspect ratio of the melt pool geometry, which can be influence by the local volumetric power density as well as encountering any porous surface features created on the previous beam path.

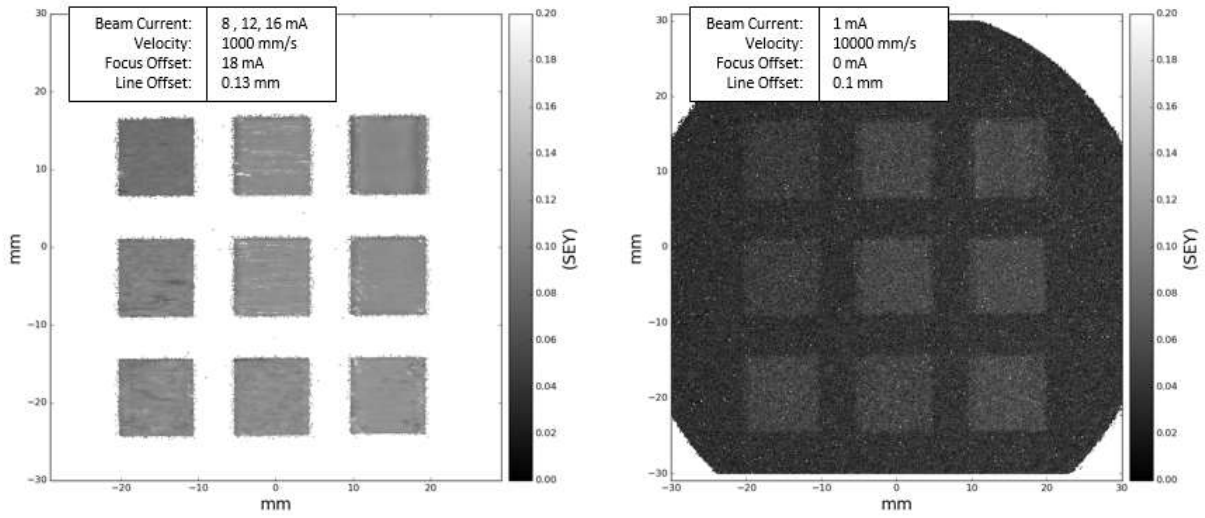

Figure 4: A comparison of Post-melt scan image and Melt image of a single layer

Stacked SEY images, cross section microscopy, and Micro CT data shown in Fig 5 reveals interconnected porosity with in the porous samples that formed the tunnel structure described by Lodes *et al.* (2015) [11] in copper, as well as by Schwerdtfeger *et al.* (2012) [15] in Ti-6Al-4V. Bauereiß *et al.* (2014) [16] investigate numerically on this issue and theorized that a low implemented beam energy leads to start of the initial defect. Pobel *et al.* (2019) [5] from the same group, propose that the main mechanism is the surface tension of the molten material, which leads to melt drops coalesces to the first surface it comes in contact with; at macro scale, the melt would preferentially bind to the walls of the previously-formed defects and eventually cause the formation of interconnected porosity. These structures are the result of surface features greater than the spot size of the beam, which in the case of the ARCAM A2 is roughly 200μm. With a line offset of 0.1mm each passes of the beam would overlap all of the solid created from the previous scan path, which measures to be 600μm using a single wafer melt line at 8mA. This overlapping of scan pattern would contribute to the visibility of many surface features, essentially performing SEM imaging over solid parts.

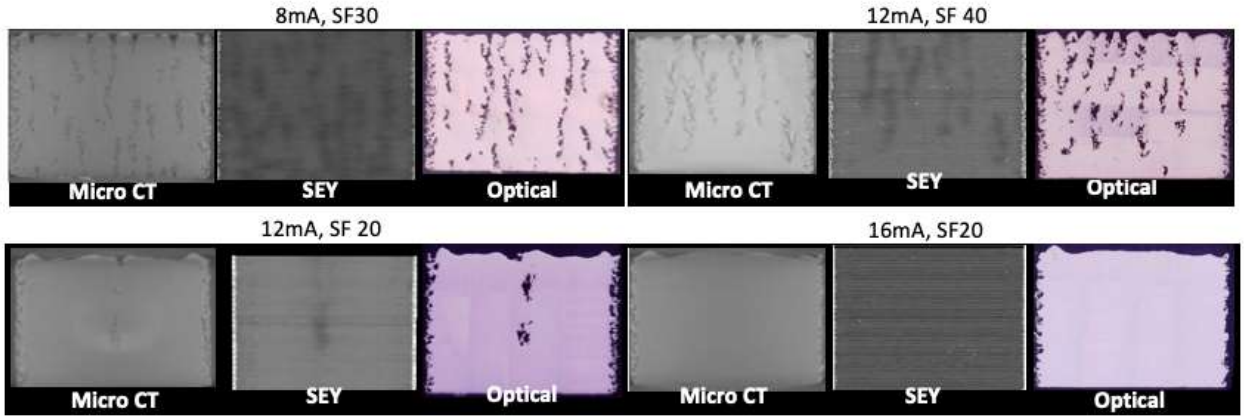

Figure 5: SEY stacked, Micro CT, and Optical image comparison.

3.2. Beam velocity Visualization

The ability to acquire the spatial-temporal correlation of the melting process allows us to map any in-situ monitored data with the associated machine parameters, and for this study we use the density derived from the electron image results to construct a similar power verse volumetric density correlation along with the data from all the previous copper parameter development efforts. During parameter development volumetric energy density is often used as a process metric, since it represents the ranges of energy input verses the time frame, and volume over which it was applied. Volumetric Energy Density, E_l, described in Equation 2, is calculates from and power *P*, as a product of acceleration voltage *U* and beam current *I*, divided by beam velocity *v, the beam overlap or hatch spacing (h), and the layer thickness(t)*. Note that this approach is somewhat arbitrary, and discounts important parameters such as beam spot size.

$$E_i = \frac{UI}{vht} \tag{2}$$

We performed two DOE builds that yields 12 samples with the speed function and turning points function on, in order to demonstrate an accelerated parameters development process. Fig 6 (a) shows the collection of SEY topo images of these 12 samples at 5 mm layer height, ranging from 8, 12 and 16 mA, and the in combination with speed function shown in Fig 6 (b) ranging from 10, 20, 30, and 40, starting with a base speed setting of 1000mm/s. This shows the relationship between current input and speed function calculation, note that the beam current is subject to the effect of the power analyzer, which is set at a surface temperature of 600C. Samples with speed function set at 10 failed both at 12 mA and 16 mA, where the thermal model regulates the beam velocity that yield a volumetric energy of 320 J/mm^3 or beyond on the edge of the samples, resulted swelling, which can be identified from the SEY images taken during melt. Sample with 12 mA and speed function of 20 present an interesting case where the center exhibit interconnected porous, yet the edge swelled due to excessive heat, in this particular scenario the window for a suitable beam velocity is above 1000 mm/s but it is an imperfection on the surface of the copper build plate that seeded the surface pours. The surface porous formed on the edge of beam current 123 mA and speed function of 40 matches the regions where the turning points function was taken into effect yet does not appear uniformly along the edges horizontal to the rake. Note that the parameter used for the machine's calculation was that the standard ARCAM recommended parameter for Ti-6Al-4V, and the current parameter development effort of copper had not incorporated the turning points function. The speed function acting to maintain a constant melt pool size performed better at greater values as evident in Fig 6 (c), where it shows the respective volumetric energy calculated by dividing Equation 2, using a hatch of 130 μm and a layer height of 40 μm.

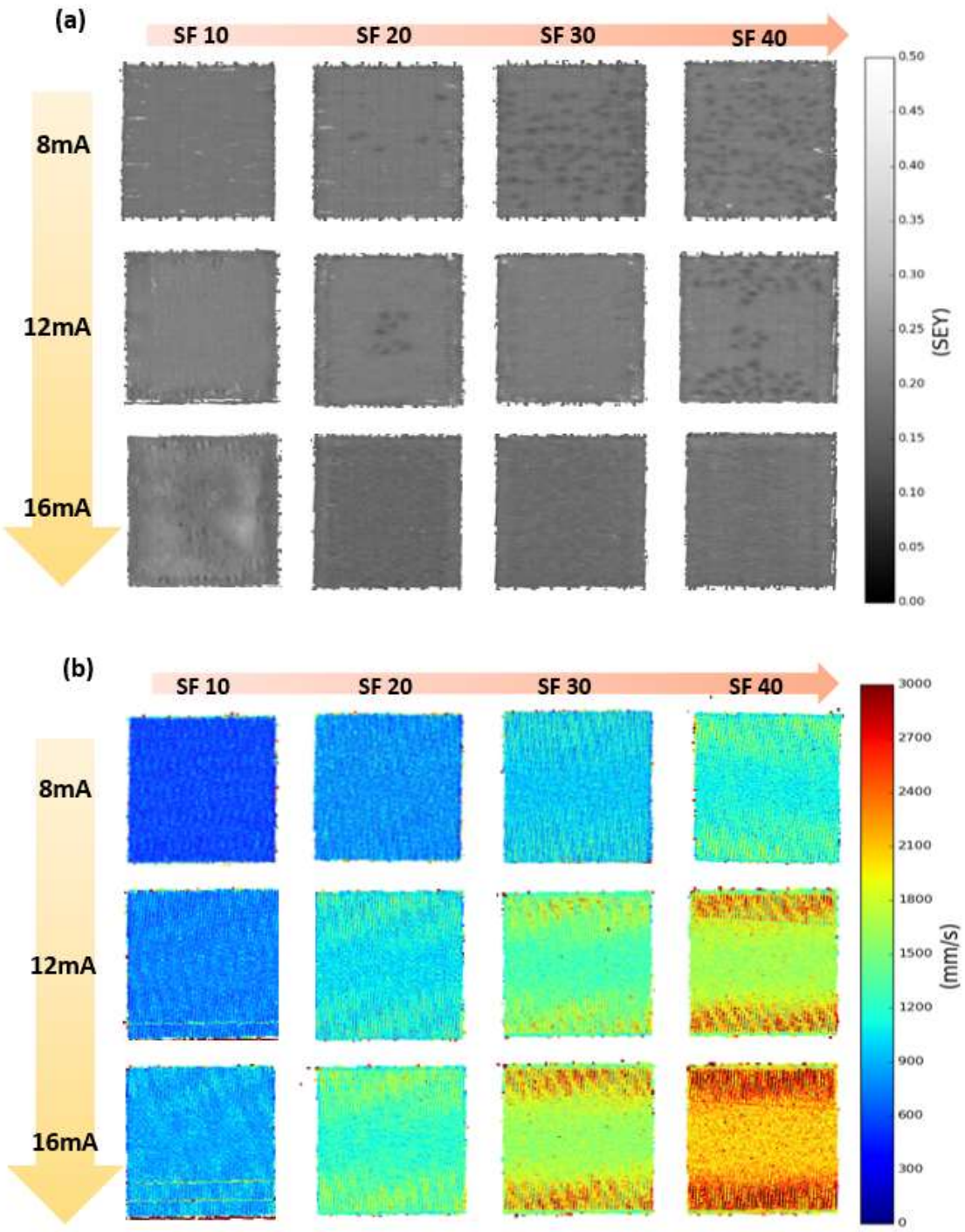

Figure 6: (a) Collections of SEY images in 8, 12, and 16 mA beam current in combination with speed function of 10, 20, 30, and 40, 8mm in layer height. (b) Respective velocity layer images,

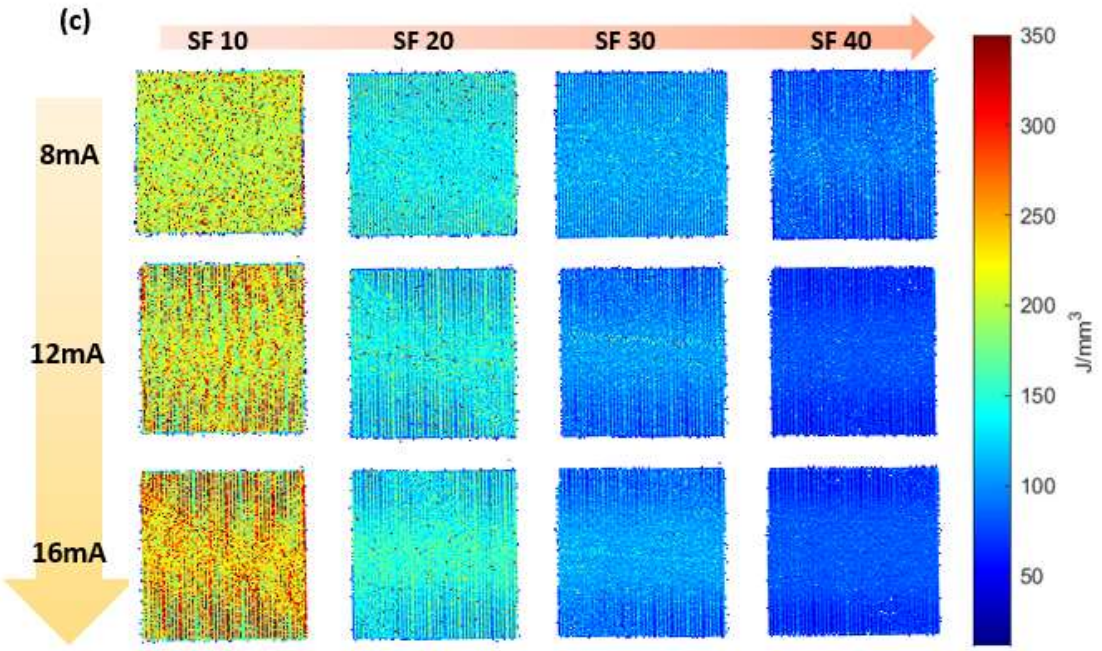

Figure 6: (c) and volumetric energy layer images

Fig 7 shows the explored volumetric energy space performed by the 12 successful DOE builds plotted along with previous pure copper EBM fabrication efforts. The density indicated here is derived from the electron signals collected during the manufacturing process, where we can determine the surface condition of dense, porous, or swell by inspecting the resulted topographical images. At 960 W three samples uses speed function of 20, 30, and 40 yielded volumetric power ranging from 310 to 70 Z/mm^3, the velocity data was collected starting from the center of each sample towards the edge where the turning points function had taken into effect. With the machines beam control functions on a single sample can explore a wide range of parameter space instead of a single data point, and this is also a closer representation of an industrial AM fabrication scenario, where beam parameter needs to be constantly adjusted for part geometry. Note that this representation of the volumetric energy space does not encounters the changes in the thermal

conductivity of the material, which is subject to change as powder material transition into solid as it's being sintered. The blue region encapsulates well performing parameter sets that can produce dense (+99.9%) copper samples, note that it crosses several volumetric energy levels, from 50 J/mm^3 to 310 J/mm^3. This region is also expected to change as the thermal conductivity of the material changes, which calls for a 3D representation of a complete parameter space in the power, volumetric velocity, and thermal conductivity axis.

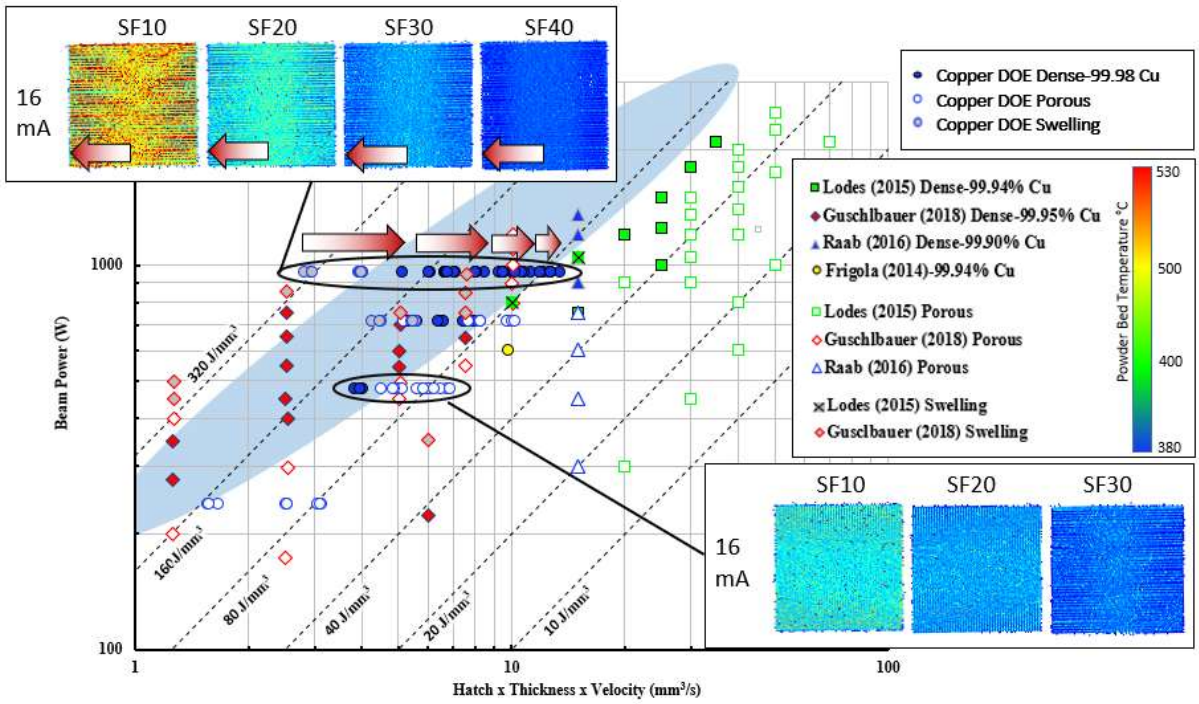

Figure 7: Volumetric energy density plot of pass copper parameter development efforts, gradient arrows indicating the changes in volumetric energy due to turning points function at 16 mA DOE samples.

Another use for velocity visualization is to see the transition for the thickness function. Fig 8 (a) shows the stacked velocity model from a generic, s-band wave guide design printed in pure

copper, where the images generated from 1094 individual layers were stacked and interpolated between the 40 μm layer heights. The design requires printing directly on top of sintered powder to form internal RF wave guide components without the use of support structures, this is achieved with the adjustment of the beam velocity via the thickness function to prevent evasive energy input on a sintered powder surface. At the bottom of the overhang region the function accelerated the beam velocity to around 7000 mm/s, declined over 2 mm of thin overhang structure, and dropped abruptly back to 740 mm/s when reached 4 mm . In the thickness function properties described by Smith *et al* (2016) (17), the three tuning parameter for altering the beam velocity within the thickness function are the speed factor S_f, thickness factor T_f,, and the exponent factor E_f,. Together they create a one dimensional velocity profile V, based on the original beam velocity, V_0, which is subject to change under different beam current and speed function. In the case of this build sample they are set at 25, 0.7 mm, and 0.4 mm^{-1} respectively, while acting on a max thickness of 4 mm. This can be calculate with the equation describe by Smith *et al* (2016) (17):

$$\frac{V}{V_0} = 1 + \frac{S_f}{\exp\left(E_f(T - T_f)\right) + 1} \tag{3}$$

With the ability to see the direct result of the altered velocity we can not only visualize such changes on the build model but observe deviation from the calculated result of the thickness function, shown in Fig 8 (b), suggesting another multiplier variable within the machine function.

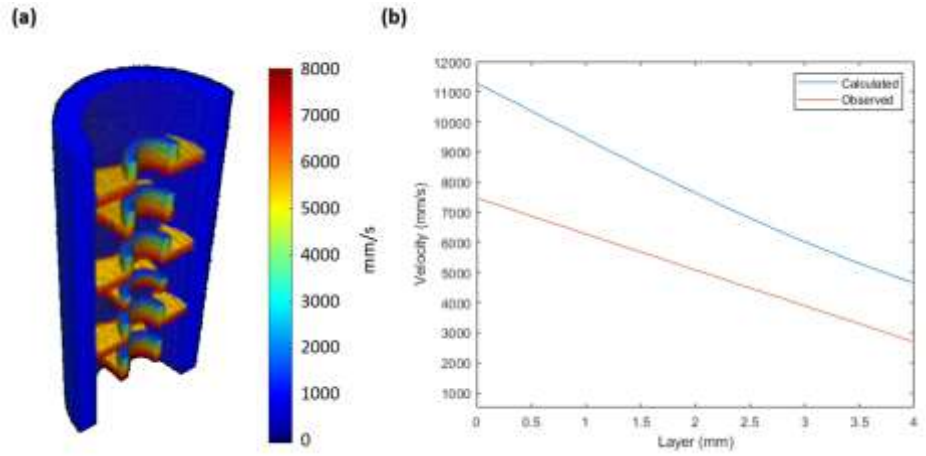

Figure 8: (a) Stacked images showing changes of beam velocity over the overhang regions on a copper s-band cavity(b) Calculated and observed beam velocity of the overhang region.

4. Discussion

During the data acquisition process noise was observed in the XY deflection coil feedback voltage, which would be translated into a higher velocity estimation if each distance were to be calculated from the linear correlation of voltage and length across the build plate. To mitigate this, we under sample the data during the signal process procedure by averaging a certain number of data points *J* and verified using turning points function images (Fig 9 (top)). Knowing that the turning points function occurs on the very edge of a model the series of images portraits the optimal amount of under sampling frequency without significant amount of spatial distortion. The spatial and sampling frequency relationship is also closely related to the beam velocity that the image is intended to illustrate, such correlation is portrayed in Fig 9 (bottom), where the amount of spatial resolution for the velocity calculation as a function of the local beam velocity are drowned at different rate of under sampling. The accuracy of the velocity measurement is benchmarked by turning off the power analyzer function, which disables any affirmation beam control functionalities, and perform sampling using varying beam speed settings.

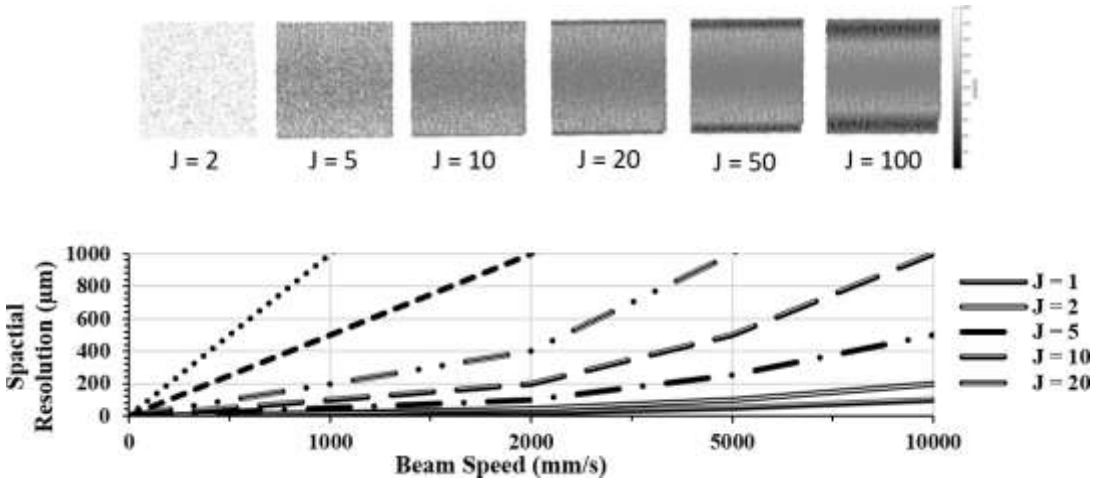

Figure 9: top: Visualizing the effect of different averaging solutions. bottom: Resolution of different averaging solutions.

SEE signal acquired during the EBM process is heavily influenced by the magnetic condition of the machine environment. The melt imaging procedure is insensitive to the external magnetic influences on the electron gun, unlike the post-melt scan, it can only image the coordinates of the intended beam location not where it actually is. A simple example demonstrated by changing the beam path with a magnet during a demonstration build of a cylindrical geometry. Fig 11 (a) shows the complete build with major build defect of shifted geometry, compared with the stacked SEY image on the Fig (b), where such change in the beam path was not detected and only porosity on the surface were shown. This is not an issue for a post melt scan of the surface where the shift would be picked up by the imaging procedure itself, and as shown by Wong *et al* (2018a) [9], was able to be used as a method of dimensional accuracy measurement. Second, like the vacuum chamber of scanning electron microscopes, the number of electrons reaching the detector is dependent on the internal charge characteristics of the chamber. Opening the viewport for instance changes this condition and hence the signal, as shown in Fig 11 (c) and (d). Lastly, the effect of smoke events where the powder was not sintered enough to overcome the repulsive force between charged

powder particles were also observed and found that they would correspond to a shift toward negative current flow, passing from the build platform to the detector. It is difficult to use this characteristic to measure the resistivity of the powder bed in-situ since it would involve isolating the build platform, although it has the potential of using it as a control system input. On the other hand, efforts into using the SEE signal collected during the preheat stage to determine the optimal sintering condition of the bed was inconclusive, as the difference in density is too minute to be distinguishable.

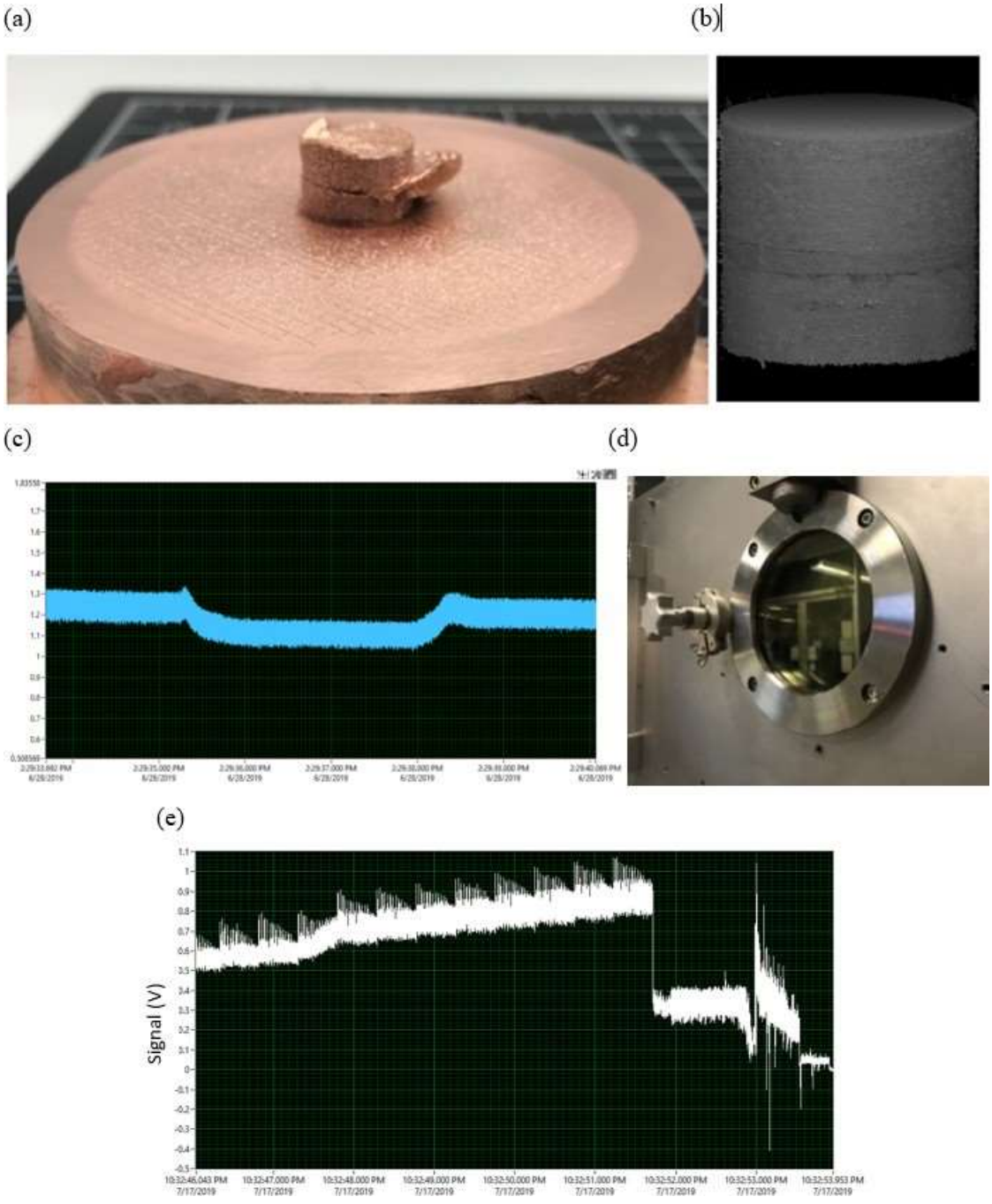

Figure 11: (a) Photo of the build sample affected by external magnetic field, (b) Stacked image of the SEY image on the affected build, (c) Electron signal during the opening of the side view port, (d) Side view port of the ARCAM A2, (e) Captured electron signal during a smoked event

5. Conclusion

With the introduction of electron optics, comes with an entire new way of studying the melt pool condition of the EBM system. Signals from melt pool created from a higher power input create spatters that reflects in higher SNR, this would theoretically happen if the incoming beam encounters the powder material before it reaches the build plate. In this case the single ejecta would be electrically isolated with the rest of the machine and during the interaction of an incident electron, where the only path to neutral for the BSE or SE created during the process is the detector plate. The effect of metallization of the detector plates is in theory, negated since it is the passing of current that is being measured instead of the voltage potential. On the other hand, the inherent flaw of using the deflection coil data for image generation is that cannot account beam shifting issues caused by external magnetic field influences, shown in Figure The SEY stacked image cannot be a treated as a quick alternative for CT, it currently can provide 250 by 250 μm resolution whereas the CT device used for this research can provide up to 13 by 13 μm. With each constituent layer being essentially a topological map of the surface, a zenith point caused by warpage would also represent a drop in SEY, as the bulging surface creates greater scattering angles. This suggest that SEY imaging of the melting process can be used as an estimation for relative density measurement, althoughthe resolution is restricted to the size of the beam.

References

[1] H. Wong, D. Neary, E. Jones, P. Fox, C. Sutcliffe, Pilot capability evaluation of a feedback electronic imaging system prototype for in-process monitoring in electron beam additive manufacturing, The International Journal of Advanced Manufacturing TechnologyC:5FN3LW7et al. - 2018 - Pilot capability evaluation of a feedback electron.pdf (2018). doi:10.1007/s00170-018-2702-6.

[2] Q. Y. Lu, C. H. Wong, Additive manufacturing process monitoring and control by non-destructive testing techniques: challenges and in-process monitoring, Virtual and Physical Prototyping 13 (2) (2018) 39–48. doi:10.1080/17452759.2017.1351201.

[3] P. E. Wollenhaupt, S. Stecker, Electron beam layer manufacturing using scanning electron monitored closed loop control, C:VEQTAUZand Stecker - 2014 - Electron beam layer manufacturing using scanning e.pdf (2014).

[4] C. Arnold, C. Pobel, F. Osmanlic, C. Körner, Layerwise monitoring of electron beam melting via backscatter electron detection, Rapid Prototyping Journal 24 (8) (2018) 1401–1406, C:3RWXTet al. - 2018 - Layerwise monitoring of electron beam melting via .pdf. doi:10.1108/RPJ-02-2018-0034.

[5] C. R. Pobel, C. Arnold, F. Osmanlic, Z. Fu, C. Körner, Immediate development of processing windows for selective electron beam melting using layerwise monitoring via backscattered electron detection, Materials LettersC:CGB4NQMet al. - 2019 - Immediate development of processing windows for se.pdf (2019). doi:10.1016/j.matlet.2019.03.048.

[6] H. Wong, D. Neary, E. Jones, P. Fox, C. Sutcliffe, Pilot feedback electronic imaging at elevated tem- peratures and its potential for in-process electron beam melting monitoring, Additive Manufacturing 27 (2019) 185–198, C:JTDLDC6et al. - 2019 - Pilot feedback electronic imaging at elevated temp.pdf. doi:10.1016/j.addma.2019.02.022.

[7] H. Wong, D. Neary, E. Jones, P. Fox, C. Sutcliffe, Pilot Attempt to Benchmark Spatial

Resolution of an Electronic Imaging System Prototype for In-Process Electron Beam Melting Monitoring (2019) 24C:DNVZLD4et al. - 2019 - Pilot Attempt to Benchmark Spatial Resolution of a.pdf.

[8] P. R. Carriere, Preliminary Investigations into the Evaporation Process using a High Brightness Electron Beam Gun 178C:8- Preliminary Investigations into the Evaporation Pr.pdf.

[9] Suppression of secondary electron yield by micro-porous array structure, Journal of Applied Physics 113 (7) (2013) 074904, C:5BPNQ98013 - Suppression of secondary electron yield by micro-p.pdf. doi:10.1063/1.4792514.

[10] D. Gamzina, N. C. Luhmann, C. Ledford, T. Horn, I. Karakaut, L. Lin, P. Frigola, Additive vacuum electronics: Electron beam melting of copper, C:38MUI46et al. - 2017 - Additive vacuum electronics Electron beam melting.pdf (2017). doi:10.1109/IVEC.2017.8289495.

[11] M. A. Lodes, R. Guschlbauer, C. Körner, Process development for the manufacturing of 99.94% pure copper via selective electron beam melting, Materials Letters 143 (2015) 298–301, C:5VMUUet al. - 2015 - Process development for the manufacturing of 99.94.pdf. doi:10.1016/j.matlet.2014.12.105.

[12] S. J. Raab, R. Guschlbauer, M. A. Lodes, C. Körner, Thermal and Electrical Conductivity of 99.9% Pure Copper Processed via Selective Electron Beam Melting: Conductivities of Pure SEBM-Copper, Advanced Engineering Materials 18 (9) (2016) 1661–1666, C:94XFXNMet al. - 2016 - Thermal and Electrical Conductivity of 99.9% Pure .pdf. doi:10.1002/adem.201600078.

[13] R. Guschlbauer, S. Momeni, F. Osmanlic, C. Körner, Process development of 99.95% pure copper processed via selective electron beam melting and its mechanical and physical properties, Materials Characterization 143 (2018) 163–170, C:et al. - 2018 - Process development of 99.95% pure copper pro cesse.pdf. doi:10.1016/j.matchar.2018.04.009.

[14] T. Horn, I. Karakurt, C. Ledford, M. Gonzalez, D. Gamzina, N. C. Luhmann, L. Lin, Additively manufactured WR-10 copper waveguide, C:76Z6Y8Bet al. - 2018 - Additively manufactured WR-10 copper waveguide.pdf (2018). doi:10.1109/IVEC.2018.8391526.

[15] J. Schwerdtfeger, R. F. Singer, C. Körner, In situ flaw detection by IR-imaging during electron beam melting, Rapid Prototyping Journal 18 (4) (2012) 259–263, C:et al. - 2012 - iIn situi flaw detection by IR-imaging during.pdf. doi:10.1108/13552541211231572.

[16] A. Bauereiß, T. Scharowsky, C. Körner, Defect generation and propagation mechanism during addi- tive manufacturing by selective beam melting, Journal of Materials Processing Technology 214 (11) (2014) 2522–2528, C:8MRDß et al. - 2014 - Defect generation and propagation mechanism during.pdf. doi:10.1016/j.jmatprotec.2014.05.002.

[17] C.J. Smith, F. Derguti, E. Hernandez Nava, M. Thomas, S. Tammas-Williams, S. Gulizia, D. Fraser, I. Todd, Dimensional accuracy of Electron Beam Melting (EBM) additive manufacture with regard to weight optimized truss structures, Journal of Materials Processing Technology, Volume 229, 2016, Pages 128-138, ISSN 0924-0136, https://doi.org/10.1016/j.jmatprotec.2015.08.028.

CHAPTER 5: Summary and future work

EBM process are capable to produce geometrically complex parts that traditional machining methods cannot achieve, the powder bed mechanism allows for a finer resolution that can meet the requirements for medical and aerospace applications. Nonetheless, the lack of process stability and repeatability due to the lack of in-situ sensing capability is still present in many industrial solutions; defects such as lack of fusion and trapped gas porosity are process related and can be mitigate by altering the input parameters by processing real time sensory inputs (Mani *et al*., 2015,Everton *et al*, 2016). Existing build monitoring technologies for EBM in most cases would involve direct optical paths to the build surface, where the quality of the alignments, the thermionic nature of the gun, and the protection necessary against metallization introduce physical limitations to their applications.

The emerging electron imaging technology for the EBM process had proven to be an easy to adapt add-ons for the existing ARCAM systems, using metal plates, amplifiers, data acquisition device, and a means of constructing the image from the signal, it is possible to build a monitoring system for during melt as well as for post melt layer scans. Chapter 3 provide details on the development of the electron imaging hardware; by applying the principle of SEM and the result from the Monti Carlo CASINO software that outlines the requirements for the operational limits of the electron signals, images were constructed with the PLC deflection coil signal and the amplified current from the electron detector.

Experiment on the melt pool signal indicates a power input to noise relationship as the low velocity, high current input to a solid surface creates spatters that results in low SNR. Using the XY location derive from the deflection coil control voltage enables the observation of the ARCAM speed and turning point function which dynamically adjust the beam speed that result in

variations in local PV values. Stacking of the individual layers of melt image provides insight to the thickness function which accounts for part sections that are directly on top of powder thus result in lower density. Chapter 3 also experiment with the design of twin detector plat plus a third noise plate, while making differential measurement between the two resulted in a higher SNR, on the other hand, the Boolean signal of the twin detector plate enables topographic or compositional mode.

During the trial and error period of this research many new designs spawn from the attempt of acquiring a better signal, as well as process technique with the hopes of producing images comparable to conventional SEM. This includes modifications that reduce the size of the detector for build area accessibility and biased detectors for enabling SE and BSE imaging mode. Another approach to this is to attach a dedicated detector plate on the rake assembly, taking advantage of the SE departing angle while compensate the smaller detector area with the proximity to the target. To further streamline the data acquisition procedure and enables future in-situ parameter change during the building process enhancements of the DAQ software or other triggering methods are needed, plus a mechanism to alter the grid cup control voltage thus to control the current during the process.

The melt pool signal intensity is the combination of powder bed condition, traces of the melt track from the previous layer and a finite amount of porosity information beneath the surface, while mix with the SE signal resulted from the plasma formed above the melt pool, and noise caused by spatter formations. With the melt pool formed ahead and solidified behind the beam spot it would be beneficial to implement the ghost beam melt strategy to probe the melt pool at the instant of its formation and transition to solid, it would require a new format of data processing procedure that can registered the abrupt change in beam current as well as new

imaging methods to differentiate the overlapping data points. Another potential application for the post melt scan is to use it as an electron channeling contrast imaging (ECCI) device. The most common way to observe dislocations is with thin film transmission electron microscope (TEM) employing diffraction contrast imaging, while ECCI offers the ability to observe bulk material with significant advantage over TEM with its non-destructive approach (Joy, 1989, Kamaladasa and Picard, 2010, Smith *et al*., 2016). Without a motorized stage in an SEM setup ECCI in EBM would extremely restricted but would be possible with larger grain structures that happens to be in the right orientation, while comparing signals from multiple detectors located in at the rack position.

To further understand the e-beam electron interaction with a powder bed surface Chapter 4 explore the possibility of using the preheat sequence to measure the state of sintering of the powder bed. With the layer scan result showing a copper bed electron signals at around 50% of the copper solid parts, it was theorized that the preheat sequence could reveal the state of sintering of the powder bed. In order to isolate the variations contributed by the beam current the exact current output at any given time must be extracted from the grid control voltage signal, hence a function was derived from the two with multiple observations on scan lines at gradient current setting. The resulting detector efficiency η_d was later plotted throughout the preheat sequence and the predicted positive trend in η_d is found to be negative. Such correlation can be contribute to the charge transfer rate of the surface material but with the grid control voltage being both time and process sensitive, the actual beam current would be effect by variables such as cathode temperature (time sensitive component), and the metallization of the grid cup (process sensitive), etc. To truly capture the gradient of sintering and its effect to the electron optics the transition

from sinter powder to solid must be observed, and a more definitive method to derive the actual outputting beam current.

Optimally, to derive process oriented feedback information of the surface condition, procedures for fast response data processing along with techniques to alter the machine parameter on-the-fly would be imperative for industrial applications. With the current understanding of the electron sensing capability in the EBM machine, possible control loops include: 1. Keyhole creation as the beam is building directly on top of powder, which would reflect on a reduced BSE/SE signal. 2.Smoke events had been observed to exhibit a change in the direction of the current flow in a very short timeframe, such an ability would be beneficial when apply as a control input for the preheat sequence. 3.Powder spread condition monitoring can be establish by the signal difference in melting or preheating on powder and on solid, this along with the ability to dynamically adjust the powder feeder dosage would allow even more autonomy to the machine's operation.

REFERENCES

ASTM Standard F2792-12, “Terminology for Additive Manufacturing Technologies.” ASTM International. https://www.astm.org/DATABASE.CART/HISTORICAL/F2792-12.htm

ASTM Standard B311-17, “Standard test methods for density of powder metallurgy (PM) materials containing less than two percent porosity.” ASTM International. https://compass.astm.org/EDIT/html_annot.cgi?B311

ASTM Standard B962-17, “Standard test methods for density of compacted or sintered powder metallurgy (PM) products using Archimedes’ principle.” ASTM International. https://compass.astm.org/EDIT/html_annot.cgi?B962+17

ARCAM A2 manual, ARCAM, http://www.arcam.com/wp-content/uploads/Arcam-A2.pdf

Abd-Elghany and Bourell, (2012), “Property Evaluation of 304L Stainless Steel Fabricated by Selective Laser Melting.” *Rapid Prototyping Journal* 18, no. 5, emealdinsight, https://www.emeraldinsight.com/doi/full/10.1108/13552541211250418

Arnold, Pobel, Osmanlic, and Körner, (2018),“Layerwise Monitoring of Electron Beam Melting via Backscatter Electron Detection.” *Rapid Prototyping Journal*, n.d., 7, emeraldinsight, https://www.emeraldinsight.com/doi/full/10.1108/RPJ-02-2018-0034

Al-Bermani, Blackmore, Zhang, and Todd, (2010), “The Origin of Microstructural Diversity, Texture, and Mechanical Properties in Electron Beam Melted Ti-6Al-4V.” *Metallurgical and Materials Transactions A* 41, no. 13, Springer, https://link.springer.com/article/10.1007/s11661-010-0397-x

Ashby M. F., (1974) "A first Report on Sintering Diagrams," Acta Met,Vol. 22, pp. 275-286, Elsevier , https://www.sciencedirect.com/science/article/pii/0001616074901679

Baumann and Reimer, (1981) “Comparison of the Noise of Different Electron Detection Systems Using a Scintillator-Photomultiplier Combination.” *Scanning* 4, no. 3, Wiley, https://onlinelibrary.wiley.com/doi/abs/10.1002/sca.4950040304

Biamino, Penna, Ackelid, Sabbadini, Tassa, Fino, Pavese, Gennaro, and Badini, (2011), “Electron Beam Melting of Ti–48Al–2Cr–2Nb Alloy: Microstructure and Mechanical Properties Investigation.” *Intermetallics* 19, no. 6, Elsevier, https://www.sciencedirect.com/science/article/pii/S0966979510004802

Boone, N., et al., (2018) “Thermal near Infrared Monitoring System for Electron Beam Melting with Emissivity Tracking,” Additive Manufacturing 22 (August 1, 2018): 601–5, https://doi.org/10.1016/j.addma.2018.06.004.

Bronshtein and Dolinin, (1968), “The secondary electron emission (SEE) of solids at large angles of incidence of primary beam,” Sov. Phys.-Solid State 9

Bruining, H., (1954), “Physics and Applications of Secondary Electron Emission.” London Pergamon Press Ltd, Elsevier, https://www.elsevier.com/books/physics-and-applications-of-secondary-electron-emission/bruining/978-0-08-009014-6

Besuelle and Nicolai, (1998), “Study of the expansion of a plasma generated by electron-beam evaporation.”, Journal of applied physics, 84(8):4114–4121, AIP, https://aip.scitation.org/doi/10.1063/1.368625

Balcon, Payan, Belhaj, Tondu, and Inguimbert, (2012), “Secondary electron emission on space materials: Evaluation of the total secondary electron yield from surface potential measurements,” IEEE Trans. PlasmaSci. 40(2), 282–290, https://ieeexplore.ieee.org/abstract/document/6069875

Berumen, Bechmann, Lindner, Kruth, and Craeghs, (2010), “Quality Control of Laser- and Powder Bed-Based Additive Manufacturing (AM) Technologies.” *Physics Procedia* 5, Elsevier,

https://www.sciencedirect.com/science/article/pii/S1875389210005158

Carriere, P.R., (2018),“Energy and Charge Transfer during Electron Beam Melting.” n.d., 259. McGill, http://digitool.library.mcgill.ca/webclient/StreamGate?folder_id=0&dvs=1558922449694~622

Crowell, C. R. (1965). "The Richardson constant for thermionic emission in Schottky barrier diodes". *Solid-State Electronics*. **8** (4): 395–399. https://www.sciencedirect.com/science/article/pii/0038110165901164

Clijsters, Craeghs, Buls, Kruth, (2014) “In situ quality control of the selective laser melting process using a high-speed, real-time melt pool monitoring system” Int J Adv Manuf Technol 75: 1089. Speinger, https://link.springer.com/article/10.1007/s00170-014-6214-8

Craeghs, Clijsters, Kruth, Bechmann, and Marie.-Christin Ebert. (2012), “Detection of Process Failures in Layerwise Laser Melting with Optical Process Monitoring.” *Physics Procedia* 39, Elseriver, https://www.sciencedirect.com/science/article/pii/S1875389212026247

Clauß, U, (2018), “Electron Beam Technology the Advanced Tool in Production,” n.d., 22, probeam, https://ewi.org/.../13-Clauss-Electron-beam-technology-the-advanced-tool-in-producti...

Clymer, Cagan, and Beuth, (2017), “Power–Velocity Process Design Charts for Powder Bed Additive Manufacturing,” *Journal of Mechanical Design* 139, no. 10, ASME, https://mechanicaldesign.asmedigitalcollection.asme.org/article.aspx?articleid=2645705

Coates, D. G., (1967), “Kikuchi-like Reflection Patterns Obtained with the Scanning Electron Microscope.” *The Philosophical Magazine: A Journal of Theoretical Experimental and Applied Physics* 16, no. 144, Taylor & Francis, https://www.tandfonline.com/doi/abs/10.1080/14786436708229968

Cordero, Z.C., *et al.*, (2017). "Powder Bed Charging during Electron-Beam Additive Manufacturing," Acta Materialia 124, Elsevier https://www.osti.gov/pages/biblio/1362208-powder-bed-charging-during-electron-beam-additive-manufacturing

Cordero, Paola, Mireles, Ridwan, and Wicker, (2017b), "Evaluation of Monitoring Methods for Electron Beam Melting Powder Bed Fusion Additive Manufacturing Technology." *Progress in Additive Manufacturing* 2, no. 1–2, Springer, https://www.springerprofessional.de/evaluation-of-monitoring-methods-for-electron-beam-melting-powde/11854786

Cunningham, Narra, Ozturk, Beuth, and Rollett, (2016), "Evaluating the Effect of Processing Parameters on Porosity in Electron Beam Melted Ti-6Al-4V via Synchrotron X-Ray Microtomography." *JOM* 68, no. 3, Springer, https://link.springer.com/article/10.1007/s11837-015-1802-0

Dehoff, R.R., Kirka, M.M., Sames, W.J., Bilheux, H., Tremsin, A.S., Lowe, L.E., Babu, S.S, (2015), "Site specific control of crystallographic grain orientation through electron beam additive manufacturing." Mater. Sci. Technol. 31 (8) (2015) 931–938. https://pdfs.semanticscholar.org/ab7c/157f77ee7963769c57100d98bb87de8ddef1.pdf

Dinwiddie, Dehoff, Lloyd, Lowe, and Ulrich, (2013), "Thermographic In-Situ Process Monitoring of the Electron-Beam Melting Technology Used in Additive Manufacturing.", Security and Sensing, SPIE Defense, https://www.spiedigitallibrary.org/conference-proceedings-of-spie/8705/87050K/Thermographic-in-situ-process-monitoring-of-the-electron-beam-melting/10.1117/12.2018412.full

Dillhoefer, Rieder, Spies, Bamberg, and Heß, (2014), "Online Monitoring of Additive Manufacturing Processes Using Ultrasound," n.d., 9, https://www.ndt.net/events/ECNDT2014/app/content/Paper/259_Spies.pdf

Danilatos, G D., (1983), “A Gaseous Detector Device for an Environmental SEM.” n.d., 12, Elsevier, https://www.sciencedirect.com/science/article/pii/004772068390002X

Danilatos and Robinson, (1979) ,“Principles of Scanning Electron Microscopy at High Specimen Chamber Pressures.” *Scanning* 2, no. 2, Wiley, https://onlinelibrary.wiley.com/doi/abs/10.1002/sca.4950020202

Danilatos, G.D., (2012) “Backscattered Electron Detection in Environmental SEM.” *Journal of Microscopy* 245, no. 2, Wiley, https://onlinelibrary.wiley.com/doi/full/10.1111/j.1365-2818.2011.03559.x

Dmitriy Trushnikov, Elena Krotova, and Elena Koleva, “Use of a Secondary Current Sensor in Plasma during Electron-Beam Welding with Focus Scanning for Process Control,” *Journal of Sensors* 2016 (2016): 1–13, https://doi.org/10.1155/2016/5302681.

Dowell, D.H., (2013) “Electron emission and cathode emittance,” n.d., 24, SLAC, http://uspas.fnal.gov/materials/10MIT/Lecture2_EmissionStatisticsCathodeEmittance_text.pdf

Doubenskaia, Pavlov, and Chivel, (May 2010), “Optical System for On-Line Monitoring and Temperature Control in Selective Laser Melting Technology.” *Key Engineering Materials* 437, Scienticif.Net, https://www.scientific.net/KEM.437.458

Eklund, Ahlfors, Bahbou, and Wedenstrand, (2018), “Optimizing HIP and Printing Parameters for EBM Ti-6Al-4V.” *Key Engineering Materials* 770, Scientific.Net, https://www.scientific.net/KEM.770.174

Everhart, T. E., (1958), “Contrast formation in the scanning electron microscope.” Phd. dissertation, Cambridge Univ., England

Everhart and Thornley, (1960), “Wide-Band Detector for Micro-Microampere Low-Energy Electron Currents.” *Journal of Scientific Instruments* 37, no. 7, IOP,

https://iopscience.iop.org/article/10.1088/0950-7671/37/7/307/meta

Everton, Hirsch, Stravroulakis, Leach, and Clare, (2016), "Review of In-Situ Process Monitoring and in-Situ Metrology for Metal Additive Manufacturing." *Materials & Design* 95, Elsevier, https://www.sciencedirect.com/science/article/pii/S0264127516300995

Everton, Dickens, Tuck, and Dutton, (2018), "Using Laser Ultrasound to Detect Subsurface Defects in Metal Laser Powder Bed Fusion Components." *JOM* 70, no. 3, Springer, https://link.springer.com/article/10.1007/s11837-017-2661-7

Everton, Dickens, Tuck, and Dutton, (2015), "Evaluation of Laser Ultrasonic Testing for Inspection of Metal Additive Manufacturing." Laser 3D Manufacturing II, SPIE, http://spie.org/Publications/Proceedings/Paper/10.1117/12.2078768

Farley and Shah, (1991), "High-Pressure Scanning Electron Microscopy of Insulating Materials: A New Approach." *Journal of Microscopy* 164, no. 2, NCBI, https://www.ncbi.nlm.nih.gov/pubmed/1774782

Furumoto, Alkahari, Ueda, Aziz, and Hosokawa, (2012), "Monitoring of Laser Consolidation Process of Metal Powder with High Speed Video Camera." *Physics Procedia* 39 https://www.sciencedirect.com/science/article/pii/S1875389212026259

Galarraga, Lados, Dehoff, Kirka, and Nandwana, (2016), "Effects of the Microstructure and Porosity on Properties of Ti-6Al-4V ELI Alloy Fabricated by Electron Beam Melting (EBM)." *Additive Manufacturing* 10, Elsevier, https://www.sciencedirect.com/journal/additive-manufacturing

Galati and Iuliano, (2018), "A Literature Review of Powder-Based Electron Beam Melting Focusing on Numerical Simulations." *Additive Manufacturing* 19: 1–20, Elsevier, https://www.sciencedirect.com/science/article/pii/S2214860417300635

Grasso, M., and Colosimo, B.M., (2017), “Process Defects and in Situ Monitoring Methods in Metal Powder Bed Fusion: A Review,” Measurement Science and Technology 28, no. 4: 044005, https://doi.org/10.1088/1361-6501/aa5c4f.

Goldstein, J., *et al.*, (2003) “Scanning Electron Microscopy and X-ray Microscropy, 3rd Edition” Kluwer Academic Publishers, New York (2003) ISBN 0306472929.

Gong H, Rafi K, Gu H, *et al*. (2014), “Analysis of defect generation in Ti-6Al-4V parts made using powder bed fusion additive manufacturing processes.” Addit Manuf. 2014;1–4:87–98. https://www.sciencedirect.com/science/article/pii/S2214860414000074

Gong H, Rafi K, Gu H, *et al*. (2015), “Influence of defects on mechanical properties of Ti-6Al-4V components produced by selective laser melting and electron beam melting.” Mater Des. 2015;86:545–554. https://digitalcommons.georgiasouthern.edu/manufact-eng-facpubs/6/

Gong, X., Cheng, B., Price, S., and Chou, K., (2013), “Powder-bed electron- beam-melting additive manufacturing: powder characterization, process simulation and metrology.” *Proc. of the ASME District F Early Career Technical Conf.* pp 59–66. https://www.researchgate.net/publication/275960612_Powder-bed_electron-beam-melting_additive_manufacturing_Powder_characterization_process_simulation_and_metrology

Goldstain, J. (Ed(s).). (2003), “Scanning electron Microscopy and X-ray Microscopy” 3rd, Springer, https://www.springer.com/us/book/9780306472923

Gunenthiram, Peyre, Schneider, Dal, Coste, and Fabbro, (2017), “Analysis of Laser–Melt Pool–Powder Bed Interaction during the Selective Laser Melting of a Stainless Steel.” Journal of Laser Applications 29, no. 2, LIA, https://lia.scitation.org/doi/10.2351/1.4983259

Gong, Rafi, Starr, and Stucker, (2013), “The Effects of Processing Parameters on Defect Regularity in Ti-6Al-4V Parts Fabricated By Selective Laser Melting and Electron Beam Melting,” n.d., 16, 24th SSF,

https://www.researchgate.net/publication/272167481_The_Effects_of_Processing_Parameters_on_Defect_Regularity_in_Ti-6Al-4V_Parts_Fabricated_By_Selective_Laser_Melting_and_Electron_Beam_Melting

Ishimoto, T., Hagihara, K., Hisamoto, K., Sun, S.H., Nakano, T.,(2017), “Crystallographic texture control of beta-type Ti–15Mo–5Zr–3Al alloy by selective laser melting for the development of novel implants with a biocompatible low Young's modulus.” Scr. Mater. 132 (2017) 34–38. https://www.sciencedirect.com/science/article/pii/S1359646216306376

Helmer, H., Bauereiß, A., Singer, R.F., Körner, C., (2016), “Grain structure evolution in Inconel 718 during selective electron beam melting.” Mater. Sci. Eng. A 668 (2016) 180–187. https://www.sciencedirect.com/science/article/abs/pii/S0921509316305536

Howell, Brad, Jared, Howell, Jeffrey, and Bradley, (2015), "Defect Characterization for Material Assurance in Metal Additive Manufacturing.", SSF, Sandia National Lab, U.S. https://www.osti.gov/biblio/1296525-defect-characterization-material-assurance-metal-additive-manufacturing

Herzog, Bechmann, Berumen, Kruth, Craeghs, (1995) “Method for Producing a Three-Dimensional Component.” Patent WO1996008749 A3, https://patents.google.com/patent/WO1996008749A3/en

Haehnel and Dade, (2008) “Physics of Particle Entrainment Under the Influence of an Impinging Jet.” n.d., 9, SemanticScholar, https://www.semanticscholar.org/paper/Physics-of-Particle-Entrainment-Under-the-Influence-Haehnel-Dade/bf3c0dfaaeef23122f9e6d7099e90bcbc044e86f

Hueso, Vicente, Gimino, Boria, Marini, and Raroncher, (2010), “Multipactor effect analysis and design rules for wedgeshaped hollow waveguides,” IEEE Trans. Electron Devices 57(12),3508–3517, https://ieeexplore.ieee.org/document/5599857

Jamshidinia and Kovacevic, (2015), “The Influence of Heat Accumulation on the Surface Roughness in Powder-Bed Additive Manufacturing.” *Surface Topography: Metrology and Properties* 3, no. 1, IOP, https://iopscience.iop.org/article/10.1088/2051-672X/3/1/014003

Jamshidinia, M., et al., (2015), “Microstructural Modification of Ti–6Al–4V by Using an in-Situ Printed Heat Sink in Electron Beam Melting® (EBM),” Journal of Materials Processing Technology 226 (December 2015): 264–71, https://doi.org/10.1016/j.jmatprotec.2015.07.006.

Joy, D.C., (1989), “Electron Channeling Patterns,” in *Techniques in Physics,* vol. 12, Elsevier, 18, https://doi.org/10.1016/B978-0-12-353855-0.50009-9.

Kamaladasa, R.J., and Picard, Y.N., (2010), “Basic Principles and Application of Electron Channeling in a Scanning Electron Microscope for Dislocation Analysis” https://www.semanticscholar.org/paper/Basic-Principles-and-Application-of-Electron-in-a-Kamaladasa/b678fd2bf57de97f6c7775b779971d7bc8478584

Kang, S.L. (2005) “Sintering: Densification, Grain Growth and Microstructure,” Elsevier, Butterworth Heinemann, Ch4 https://www.elsevier.com/books/sintering/kang/978-0-7506-6385-4

Kawrakow, I., (2000), “Accurate Condensed History Monte Carlo Simulation of Electron Transport. II. Application to Ion Chamber Response Simulations.” *Medical Physics* 27, no. 3 , NCBI, https://www.ncbi.nlm.nih.gov/pubmed/10757602

Kanaya and Okayama, (1972). “Penetration and energy-loss theory of electrons in solid targets.” *J. Phys. D: Appl. Phys.* **5**, 43–58. IOP Science, https://iopscience.iop.org/article/10.1088/0022-3727/5/1/308/meta

King WE, Barth HD, Castillo VM, *et al*., (2014), "Observation of keyhole-mode laser melting in laser powder-bed fusion additive manufacturing.", J Mater Process Technol. 2014;214:2915–2925. https://www.sciencedirect.com/science/article/pii/S0924013614002283

Klassen, A. (2017), "Simulation of Evaporation Phenomena in Selective Electron Beam Melting," n.d., 269, FAU https://opus4.kobv.de/opus4-fau/files/9756/AlexanderKlassen_Diss_OPUS.pdf

Knowles, Hardt and Smith, (1999), "Gaseous backscattered electron detector for an environmental scanning electron microscope." U.S. Patent 5945672A, https://patents.google.com/patent/US5945672

Krishna Chaitanya Nune, Shujun Li, and R. Devesh Kumar Misra, "Advancements in Three-Dimensional Titanium Alloy Mesh Scaffolds Fabricated by Electron Beam Melting for Biomedical Devices: Mechanical and Biological Aspects," *Science China Materials* 61, no. 4 (April 2018): 455–74, https://doi.org/10.1007/s40843-017-9134-x.

Kleszczynski, S., zur Jacobsmühlen, J., Sehrt, J.T., and Witt, G., (2012), "Error detection in laser beam melting systems by high resolution imaging." *Proc. of the Solid Freeform Fabrication Symp. http://sffsymposium.engr.utexas.edu/Manuscripts/2012/2012-74-Kleszczynski.pdf*

Kok, Y.,et al., (2018) "Anisotropy and Heterogeneity of Microstructure and Mechanical Properties in Metal Additive Manufacturing: A Critical Review," Materials & Design 139 (February 2018): 565–86, https://doi.org/10.1016/j.matdes.2017.11.021

Kanter, H., (1961), "Contribution of Backscattered Electrons to Secondary Electron Formation." *Physical Review* 121, no. 3, APS, https://journals.aps.org/pr/abstract/10.1103/PhysRev.121.681

Kimoto and Hashimoto, (1968), "On the contrast and resolution of the scanning electron microscope" Scanning Electron Microscopy 1968, IITRI, Chicago.

Kimoto**,** Hashimoto, and Suganuma, (1966), “Stereoscopic observation in scanning microscopy using multiple detectors.” The Electron Microprobe,

Karthik, N., (2013), “High Frequency Ultrasonic Non-Destructive Evaluation of Additively Manufactured Components.”, 24th International Solid Freeform Fabrication Symposium, https://pdfs.semanticscholar.org/1915/8f8af23d405e41baed2c63a4b224027e96ef.pdf

Kruth, Duflou, J., and Mervelis, (2007), “On-line monitoring and process control in selective laser melting and laser cutting”, Proceedings of the 5th Lane Conference, Laser Assisted Net Shape Engineering, Vol. 1, pp. 23-37, https://www.researchgate.net/publication/285085957_On-line_monitoring_and_process_control_in_selective_laser_melting_and_laser_cutting

Khairallah, Anderson, Rubenchik, and King, (2016), “Laser Powder-Bed Fusion Additive Manufacturing: Physics of Complex Melt Flow and Formation Mechanisms of Pores, Spatter, and Denudation Zones.” *Acta Materialia* 108, Elsevier, https://www.sciencedirect.com/science/article/pii/S135964541630088X

Lane, Mekhontsev, Grantham, Vlasea, Whiting, Yeung, Fox, *et al*., (2016), “Design, Developments, and Results from the NIST Additive Manufacturing Metrology Testbed (AMMT),” n.d., 17, NIST, https://www.nist.gov/publications/design-developments-and-results-nist-additive-manufacturing-metrology-testbed-ammt

Lane, Grantham, Yeung, Zarobila, and Fox, (2017),“Performance Characterization of process Monitoring Sensors on the NIST Additive Manufacturing Metrology Testbed,” n.d., 10, NIST, https://www.nist.gov/publications/performance-characterization-process-monitoring-sensors-nist-additive-manufacturing

Leung, Marussi, Atwood, Towrie, Withers, and Lee, (2018), “In Situ X-Ray Imaging of Defect and Molten Pool Dynamics in Laser Additive Manufacturing.” *Nature Communications* 9, no. 1, , https://www.nature.com/articles/s41467-018-03734-7

Li, Liu, Wen, He, Zhong, Wei, Shi, and Liu, (2018), “In Situ 3D Monitoring of Geometric Signatures in the Powder-Bed-Fusion Additive Manufacturing Process via Vision Sensing Methods.” *Sensors* 18, no. 4, NCMI, https://www.ncbi.nlm.nih.gov/pmc/articles/PMC5949040/

Ly, Rubenchik, Khairallah, Guss, and Matthews, (2017), “Metal Vapor Micro-Jet Controls Material Redistribution in Laser Powder Bed Fusion Additive Manufacturing.” *Scientific Reports* 7, no. 1, Science Report, https://www.nature.com/articles/s41598-017-04237-z

Liu, Yang, Mai, Wang, and Song, (2015), “Investigation into Spatter Behavior during Selective Laser Melting of AISI 316L Stainless Steel Powder.” *Materials & Design* 87, Elsevier, https://www.deepdyve.com/lp/elsevier/investigation-into-spatter-behavior-during-selective-laser-melting-of-fIUmaTPx7w

Lawerence, G., (1974) “Triode electron gun for electron beam machines.”. U.S. Patent 3,835,327, https://patents.google.com/patent/US3835327A/en

Larosa, M.A., Jardini, A.L., Zavaglia, C.A., Kharmandayan, P., Calderoni, D.R., and Filho, R.M., (2014), “Microstructural and Mechanical Characterization of a Custom-Built Implant Manufactured in Titanium Alloy by Direct Metal Laser Sintering.” Adv. Mech. Eng., vol. 2014, pp. 1–8, 2014. https://journals.sagepub.com/doi/10.1155/2014/945819

Lee, Kirka, Dinwiddie, Raghavan, Turner, Dehoff, and Babu, (2018) “Role of Scan Strategies on Thermal Gradient and Solidification Rate in Electron Beam Powder Bed Fusion.” *Additive Manufacturing* 22, Elsevier, https://www.sciencedirect.com/science/article/pii/S2214860417302439

Mladenov, G.M., et al., (2016) “Parameters and Some Applications of Plasma Generated during Keyhole Welding Using a Highly Concentrated Energy Beam – an Overview,” International Journal of Engineering Research 2, no. 3 (n.d.): 22. https://www.researchgate.net/publication/311206206_Parameters_and_some_applications_of_pla

sma_generated_during_keyhole_welding_using_a_highly_concentrated_energy_beam_-_an_overview

Mani, M., Lane, B., Donmez, A., Feng, S., Moylan, S., and Fesperman, R. , (2015), "Measurement science needs for real-time control of additive manufacturing powder bed fusion processes." *NIST Interagency/Internal Report (NISTIR)* 8036 National Institute of Standards and Technology, Gaithersburg, MD. https://www.nist.gov/publications/measurement-science-needs-real-time-control-additive-manufacturing-powder-bed-fusion

Mireles, Ridwan, Morton, Hinojos, and Wicker, (2015), "Analysis and Correction of Defects within Parts Fabricated Using Powder Bed Fusion Technology." *Surface Topography: Metrology and Properties* 3, no. 3, IOP, https://iopscience.iop.org/article/10.1088/2051-672X/3/3/034002

Mousa, A.A., (2016), "Experimental investigations of curling phenomenon in selective laser sintering process." *Rapid Prototyping J.* **22** 405–15. https://www.emeraldinsight.com/doi/full/10.1108/RPJ-12-2013-0132

Murr, Gaytan, and Medina, *et al*., (2008), "Effect of building parameters and build geometries on residual microstructures and mechanical properties of Ti-6Al-4V components build by electron beam melting(EBM)," n.d., 25, AB Arcam, https://www.researchgate.net/publication/235666959_Effect_of_build_parameters_and_build_geometries_on_residual_microstructures_and_mechanical_properties_of_Ti-6Al-4V_components_built_by_electron_beam_melting_EBM

Murr, Martinez, Gaytan, Ramirez, Machado, Shindo, Martinez, *et al*., (2011), "Microstructural Architecture, Microstructures, and Mechanical Properties for a Nickel-Base Superalloy Fabricated by Electron Beam Melting." *Metallurgical and Materials Transactions A* 42, no. 11, Springer, https://link.springer.com/article/10.1007/s11661-011-0748-2

Maldague, X.P.V., (2001), "Theory and practice of infrared technology for nondestructive testing." New York, NY: John Wiley & Sons, Inc.

https://www.scirp.org/(S(351jmbntvnsjt1aadkposzje))/reference/ReferencesPapers.aspx?ReferenceID=244328

Moll, Healey, Sullivan, Johnson, (1978), "A high efficiency, non- directional backscattered electron detection mode for the SEM." Scanning Electron Microscopy 1978, SEM Inc, AMF O'Hare, pp 303-310

Mohan, Hwu, and Joy, (2006), "Secondary Electron Imaging in the Variable Pressure Scanning Electron Microscope." *Scanning* 20, no. 6, Wiley, https://onlinelibrary.wiley.com/doi/pdf/10.1002/sca.1998.4950200603

Morgan and Phillips, (2006), "Gaseous Scintillation Detection and Amplification in Variable Pressure Scanning Electron Microscopy." *Journal of Applied Physics* 100, no. 7, AIP, https://aip.scitation.org/doi/10.1063/1.2355539

Nishio, Tuchida, Tooma, and Suzuki, (1992), "Origins of Charged Particles in Vapor Generated by Electron-beam Evaporation." *Journal of Applied Physics* 72, no. 10, AIP, https://aip.scitation.org/doi/abs/10.1063/1.352334

Napchan, E., (2001), "Backscattered Electrons in the SEM," n.d., 3, https://microscopy-analysis.com/sites/default/files/magazine_pdfs/mag%20225_2001_Jan_Napchan_1.pdf

Niedrig, H., (1978), "Physical Background of Electron Backscattering." *Scanning* 1, no. 1, Wiley, https://onlinelibrary.wiley.com/doi/abs/10.1002/sca.4950010103

Ohba, Ogura, Nishimura, Tamura, and Shibata, (2000), "Effect of Electron Beam on Velocities of Uranium Atomic Beams Produced by Electron Beam Heating." *Japanese Journal of Applied Physics* 39, no. Part 1, No. 9A, IOP, https://iopscience.iop.org/article/10.1143/JJAP.39.5347

Oltean and Abrudean, (2008), "Advanced Control of the Electron Beam Welding" Journal of Control Engineering and Applied informations, n.d., 10

http://www.ceai.srait.ro/index.php?journal=ceai&page=article&op=view&path%5B%5D=25

Oatley, C. W., (1985), "The Detective Quantum Efficiency of the Scintillator/Photomultiplier in the Scanning Electron Microscope." *Journal of Microscopy* 139, no. 2, Wiley, https://onlinelibrary.wiley.com/doi/abs/10.1111/j.1365-2818.1985.tb02632.x

Pandey, J., et al., (2013) "Application of Thermography Technique for Assessment and Monitoring of Coal Mine Fire: A Special Reference to Jharia Coal Field, Jharkhand, India," International Journal of Advanced Remote Sensing and GIS, n.d., 10. http://technical.cloud-journals.com/index.php/IJARSG/article/view/Tech-93

Paul, Anand, and Gerner, (2014),"Effect of Thermal Deformation on Part Errors in Metal Powder Based Additive Manufacturing Processes." *Journal of Manufacturing Science and Engineering* 136, no. 3: 031009, https://www.researchgate.net/publication/275379403_Effect_of_Thermal_Deformation_on_Part_Errors_in_Metal_Powder_Based_Additive_Manufacturing_Processes

Peter Petrov, Chavdar Georgiev, and Georgy Petrov, (1998) "Experimental Investigation of Weld Pool Formation in Electron Beam Welding," Vacuum 51, no. 3 (November 1998): 339–43, https://doi.org/10.1016/S0042-207X(98)00110-9.

Piňos, Mikmeková, and Frank, (2017) "About the Information Depth of Backscattered Electron Imaging: About the information depth." *Journal of Microscopy* 266, no. 3, Wiley, https://onlinelibrary.wiley.com/doi/full/10.1111/jmi.12542

Pivi, King, Kirby, Raubenheimer, Stupakov, and Pimpec, (2008), "Sharp reduction of the secondary electron emission yield from grooved surfaces." Journal of Applied Physics, 104(10):104904, AIP, https://aip.scitation.org/doi/pdf/10.1063/1.3021149?class=pdf

Pobel, Arnold, Osmanlic, Fu, Körner, (2019), “Immediate development of processing windows for selective electron beam melting using layerwise monitoring via backscattered electron detection.” Materials Letters, n.d.249, Elsevier, https://www.sciencedirect.com/science/article/pii/S0167577X19304355

Pavlov, Doubenskaia and Smurov, (2010), “Pyrometric Analysis of Thermal Processes in SLM Technology.” *Physics Procedia* 5, Elsevier, https://www.sciencedirect.com/science/article/pii/S1875389210005067

Prabhakar, P., Sames, W.J., Dehoff, R., and Babu, S.S., (2015), “Computational modeling of residual stress formation during the electron beam melting process for Inconel 718.” *Add. Manuf.* **7** 83–91. https://www.sciencedirect.com/science/article/pii/S2214860415000160

Puebla, K., Murr, L., Gaytan, S., (2012), “Effect of melt scan rate on microstructure and macrostructure for electron beam melting of Ti–6Al–4V.” Mater. Sci. 2012: 259–264. https://www.sciencedirect.com/science/article/pii/S104458031500039X

Raghavan, N, Jordan, B. H., and Dehoff, R. R., (2018) “Controlling Microstructure in Deposits Fabricated Using Powder Blown Direct Energy Deposition Technique,”, https://doi.org/10.2172/1459282.

Ramirez, Murr, Li, Tian, Martinez Martinez, Machado, Gaytan, Medina, and Wicker, (2011), “Open-Cellular Copper Structures Fabricated by Additive Manufacturing Using Electron Beam Melting.” *Materials Science and Engineering: A* 528, no. 16–17, Elsevier, https://www.sciencedirect.com/science/article/pii/S0921509311003376

Rabin, Smolik, and Korth, (1990), “Characterization of Entrapped Gases in Rapidly Solidified Powders.” *Materials Science and Engineering: A* 124, no. 1, Elsevier, https://www.sciencedirect.com/science/article/pii/092150939090328Z

Raplee, Plotkowski, Kirka, Dinwiddie, Okello, Dehoff, and Babu, (2017), "Thermographic Microstructure Monitoring in Electron Beam Additive Manufacturing." *Scientific Reports* 7, NCBI, https://www.ncbi.nlm.nih.gov/pubmed/28256595

Ramakoteswara, R.P., (2003), "Laser isotope separation of uranium." Current science, 85(5):615–633, INIS, https://inis.iaea.org/search/search.aspx?orig_q=RN:35000760

Reimer and Riepenhausen, (1985), "Detector Strategy for Secondary and Backscattered Electrons Using Multiple Detector Systems." *Scanning* 7, no. 5, Wiley, https://onlinelibrary.wiley.com/doi/pdf/10.1002/sca.4950070503
Reimer and Volbert, (1979), "Detector System for Backscattered Electrons by Conversion to Secondary Electrons." *Scanning* 2, no. 4, Wiley, https://onlinelibrary.wiley.com/doi/pdf/10.1002/sca.4950020406

Rodriguez, Medina, Espalin, Terrazas, Muse, Henry, MacDonald, and Wicker, (2012), "Integration of a Thermal Imaging Feedback Control System in Electron Beam Melting," n.d., 17, IOP, https://www.researchgate.net/publication/288530561_Integration_of_a_thermal_imaging_feedback_control_system_in_electron_beam_melting

Romano, J.P., (2015), "Thermal Transport and Melt Pool Geometry in Metallic Powder Bed Additive Manufacturing Processes for Various Novel Engineering Materials." n.d., 74. https://opencommons.uconn.edu/cgi/viewcontent.cgi?article=1937&context=gs_theses

Robinson, V N E.,(1973), "A Reappraisal of the Complete Electron Emission Spectrum in Scanning Electron Microscopy." *Journal of Physics D: Applied Physics* 6, no. 12, IOP, https://iopscience.iop.org/article/10.1088/0022-3727/6/12/101

Robinson, V. N. E., (1980), "Imaging with Backscattered Electrons in a Scanning Electron Microscope." *Scanning* 3, no. 1, Wiley,

https://onlinelibrary.wiley.com/doi/pdf/10.1002/sca.4950030103

Raghavan, N., Jordan, B.H., and Dehoff, R.R., (2018) "Controlling Microstructure in Deposits Fabricated Using Powder Blown Direct Energy Deposition Technique," June 1, 2018, https://doi.org/10.2172/1459282.

Sames, List, Pannala, Dehoff, and Babu, (2016), "The Metallurgy and Processing Science of Metal Additive Manufacturing." *International Materials Reviews* 61, no. 5: 315–60, Taylor & Francis, https://www.tandfonline.com/doi/full/10.1080/09506608.2015.1116649#

Seabra, Azevedo, Araújo, Reis, Pinto, Alves,i Santos, and Mortágua, (2016), "Selective Laser Melting (SLM) and Topology Optimization for Lighter Aerospace Componentes." *Procedia Structural Integrity* 1, Elsevier, https://www.sciencedirect.com/science/article/pii/S2452321616000408

Seidel and Johnson (1971). "Initial Sintering Kinetics of Silver", Physics of Sintering, Vol. 3, No. 3 pp 143–157 https://www.researchgate.net/publication/35952879_Initial_sintering_kinetics_of_silver

Seiler, H., (1983), "Secondary Electron Emission in the Scanning Electron Microscope." *J. Appl. Phys.* 54, no. 11, AIP, https://aip.scitation.org/doi/10.1063/1.332840

Sames, Unocic, Dehoff, Lolla, and Babu, (2014), "Thermal Effects on Microstructural Heterogeneity of Inconel 718 Materials Fabricated by Electron Beam Melting." *Journal of Materials Research* 29, no. 17: 1920–30, Cambridge Core, https://www.cambridge.org/core/journals/journal-of-materials-research/article/thermal-effects-on-microstructural-heterogeneity-of-inconel-718-materials-fabricated-by-electron-beam-melting/B58A1C9056224B73AC4F88EC9C21D07F

Shevchik, Kenel, Leinenbach, and Wasmer, (2018), “Acoustic Emission for in Situ Quality Monitoring in Additive Manufacturing Using Spectral Convolutional Neural Networks.” *Additive Manufacturing* 21, Elsevier, https://www.sciencedirect.com/science/article/pii/S221486041730132X

Shen, N., and Chou, K., (2012), “Thermal Modeling of Electron Beam Additive Manufacturing Process: Powder Sintering Effects.” ASEM 2012, pp. 1–9, 2012. https://www.researchgate.net/publication/267602021_Thermal_Modeling_of_Electron_Beam_Additive_Manufacturing_Process_Powder_Sintering_Effects

Slotwinski, Garboczi, and Hebenstreit, (2014), “Porosity Measurements and Analysis for Metal Additive Manufacturing Process Control.” *Journal of Research of the National Institute of Standards and Technology* 119, NIST, https://www.nist.gov/publications/porosity-measurements-and-analysis-metal-additive-manufacturing-process-control

Schwerdtfeger, Singer, Körner, (2012), “In situ flaw detection by IR-imaging during electron beam melting.” Rapid Prototyping Journal, Vol. 18, 4, pp. 259-263, TIB, https://www.tib.eu/en/search/id/BLSE%3ARN314146576/In-situ-flaw-detection-by-IR-imaging-during-electron/

Smith, C.J., *et al*., (2016), “Dimensional Accuracy of Electron Beam Melting (EBM) Additive Manufacture with Regard to Weight Optimized Truss Structures,” *Journal of Materials Processing Technology* 229: 128–38, https://doi.org/10.1016/j.jmatprotec.2015.08.028.

Shen and Chou, (2012), “Thermal modeling of electron beam additive manufacturing process: powder sintering effects.”, ASME 2012 International Manufacturing Science and Engineering Conference, American Society of Mechanical Engineers, pp. 287–295, https://proceedings.asmedigitalcollection.asme.org/proceeding.aspx?articleid=1717309

Sharratt, B.M., (2015), “Non-destructive techniques and technologies for qualification of additive manufactured parts and processes, A literature review.” *Contract Report* DRDC-RDDC-2015-

C035 (Victoria, BC: Sharratt Research & Consulting Inc.) http://cradpdf.drdc-rddc.gc.ca/PDFS/unc200/p801800_A1b.pdf

Spierings, A.B., Schneider, M., and Eggenberger, R., (2011) "Comparison of Density Measurement Techniques for Additive Manufactured Metallic Parts," *Rapid Prototyping Journal* 17, no. 5 (August 2, 2011): 380–86, https://doi.org/10.1108/13552541111156504.

Tammas-Williams, Withers, Todd, and Prangnell, (2017), "The Influence of Porosity on Fatigue Crack Initiation in Additively Manufactured Titanium Components." *Scientific Reports* 7, no. 1, Science Report, https://www.nature.com/articles/s41598-017-06504-5

Tammas-Williams S, Zhao H, Léonard F, *et al*., (2015), "XCT analysis of the influence of melt strategies on defect population in Ti-6Al-4V components manufactured by selective electron beam melting." Mater Charact. 2015;102: 47–61. https://www.sciencedirect.com/science/article/pii/S104458031500039X

Thijs, L., Kempen, K., Kruth, J.P.,Van Humbeeck, V., (2013), "Fine-structured aluminum products with controllable texture by selective laser melting of pre-alloyed AlSi10Mg powder." Acta Mater. 61 (5) (2013) 1809–1819. https://www.sciencedirect.com/science/article/abs/pii/S1359645412008592

Trushnikov, D.N. (2013),"Effect of Beam Deflection Oscillations on the Weld Geometry," Journal of Materials Processing Technology 213, no. 9 https://www.researchgate.net/publication/257345728_Effect_of_beam_deflection_oscillations_on_the_weld_geometry

Trushnikov, Belenkiy, Shchavlev, Piskunov, Abdullin, and Mladenov, (2012), "Attenuation and escape depths of low-energy electron emission.", Journal of Sensors, 12(12): 17433–17445, PMC, https://www.ncbi.nlm.nih.gov/pmc/articles/PMC3571846/

Trushnikov, D., Krotova, E., and Koleva, E., (2016) "Use of a Secondary Current Sensor in Plasma during Electron-Beam Welding with Focus Scanning for Process Control," *Journal of Sensors* 2016 (2016): 1–13, https://doi.org/10.1155/2016/5302681

Tabata, (2007) "Backscattering coefficients of electrons: A review" n.d., 6, Semantic Scholar https://www.researchgate.net/publication/237453145_Backscattering_coefficients_of_electrons_A_review

Tiferet, E. et al., (2019) "Mapping the Tray of Electron Beam Melting of Ti-6Al-4V: Properties and Microstructure," *Materials* 12, no. 9 (May 7, 2019): 1470, https://doi.org/10.3390/ma12091470.

Vo, T.H., Museau, M., Vignat, F., Villeneuve, F., Ledoux, Y., Ballu A., (2018) "Typology of Geometrical Defects in Electron Beam Melting," Procedia CIRP 75: 92–97, https://doi.org/10.1016/j.procir.2018.04.033.

Wang, Hu, Chen, and Pang, (2018), "Modeling Fluid Dynamics of Vapor Plume in Transient Keyhole during Vacuum Electron Beam Welding." *Vacuum* 157, Elsevier, https://www.sciencedirect.com/science/article/pii/S0042207X18311485

Wells, O.C., (1970), "New Contrast Mechanism for Scanning Electron Microscope." *Applied Physics Letters* 16, no. 4, AIP, https://aip.scitation.org/doi/10.1063/1.1653139

Wells, O.C., (1974), "Scanning Electron Microscopy." McGraw-Hill Book Co, Ch 6, https://physicstoday.scitation.org/doi/pdf/10.1063/1.3069062

Williams, D.B. (1984) "Recent Advances in the Electron Microscopy of Materials," Advances in Electronics and Electron Physics Volume 62

Wong, Neary, Shahzad, Jones, Fox, and Sutcliffe, (2018a), “Pilot Investigation of Feedback Electronic Image Generation in Electron Beam Melting and Its Potential for In-Process Monitoring.” Journal of Materials Processing Technology, Elsevier, https://www.sciencedirect.com/science/article/pii/S0924013618304527?via%3Dihub

Wong, Neary, Jones, Fox, and Sutcliffe, (2018b), “Pilot Capability Evaluation of a Feedback Electronic Imaging System Prototype for In-Process Monitoring in Electron Beam Additive Manufacturing.” *The International Journal of Advanced Manufacturing Technology*, Springer, https://link.springer.com/article/10.1007/s00170-018-2702-6

Wong, Neary, Jones, Fox, and Sutcliffe. (2019a), “Pilot Attempt to Benchmark Spatial Resolution of an Electronic Imaging System Prototype for In-Process Electron Beam Melting Monitoring.” Preprints, https://www.preprints.org/manuscript/201901.0169/v1

Wong, Neary, Jones, Fox, and Sutcliffe, (2019b), “Pilot Feedback Electronic Imaging at Elevated Temperatures and Its Potential for In-Process Electron Beam Melting Monitoring.” *Additive Manufacturing* 27, Elsevier, https://www.preprints.org/manuscript/201901.0098/v1/download

Wolf and Everhart, (1969), “Annular diode detector for high angular resolution pseudo-Kikuchi patterns.” Scanning Electron Microscopy, IITRI, Chicago.

Wollenhaupt, Phillip, and Stecker, (2014), “Electron beam layer manufacturing using scanning electron monitored closed loop control.”, U.S. Patent 8809780B2, https://patents.google.com/patent/US8598523B2/en

Xie, Xiao, and Wang, (2016) , “Formulae for the Secondary Electron Yield and Total Stopping Power from 0.8 KeV to 10 KeV for Metals.” *Pramana* 86, no. 5, Springer, https://link.springer.com/article/10.1007/s12043-015-1119-0

Yasa, E., Deckers, J., Craeghs, T., Badrossamay, M. and Kruth, J.P., (2009), “Investigation on occurrence of elevated edges in selective laser melting *Int. Solid Freeform Fabrication Symp.”*

Proc. of the Solid Freeform Fabrication Symp (Austin, TX) pp 673–85. https://pdfs.semanticscholar.org/396c/c2ff5b27151a3db4d257fe9daea3275d5e63.pdf

Ye, He, Hu, Wang, Hu, Yang and Cui, (2013): "Suppression of Secondary Electron Yield by Micro-Porous Array Structure," "Suppression of Secondary Electron Yield by Micro-Porous Array Structure," Journa*l of Applied Physics* 113, no. 7: 074904, https://doi.org/10.1063/1.4792514

Ye, Fuh, Zhang, Hong, and Zhu, (2018), "Defects Recognition in Selective Laser Melting with Acoustic Signals by SVM Based on Feature Reduction." *IOP Conference Series: Materials Science and Engineering* 436, no. 1, IOP, https://iopscience.iop.org/article/10.1088/1757-899X/436/1/012020

Yu, Lim, Smith, Babu, Farson, Lippold, and McCracken, (2014), "Reducing Hot Cracking Tendency of Dissimilar Weld Overlay by Magnetic Arc Oscillation." *Materials Science and Technology* 30, no. 8, Tayor & Francis, https://www.tandfonline.com/doi/full/10.1179/1743284713Y.0000000358

Zhao, Fezzaa, Cunningham, Wen, Carlo, Chen, Rollett, and Sun, (2017), "Real-Time Monitoring of Laser Powder Bed Fusion Process Using High-Speed X-Ray Imaging and Diffraction." *Scientific Reports* 7, no. 1 , https://www.nature.com/articles/s41598-017-03761-2

Zhang, Hu, Wang, Cao, Zhang, and Cui, (2012), "Note: Measuring effect of Ar-ion cleaning on the secondary electron yield of cop- per due to electron impact," Rev. Sci. Instrum. 83, 066105, NCBI, https://www.ncbi.nlm.nih.gov/pubmed/22755671

Zhang, Hong, Ye, Zhu, and Fuh, (2018), "Extraction and Evaluation of Melt Pool, Plume and Spatter Information for Powder-Bed Fusion AM Process Monitoring." *Materials & Design* 156, Elsevier, https://app.dimensions.ai/details/publication/pub.1105301154

Zur Jacobsmühlen, J., Kleszczynski, S., Schneider, D., and Witt, G., (2013), “High resolution imaging for inspection of laser beam melting systems.” *2013 IEEE Int. Instrumentation and Measurement Technology Conf. (I2MTC)* (IEEE) pp 707–12. https://ieeexplore.ieee.org/document/6555507

APPENDICES

Appendix A

LabVIEW UI

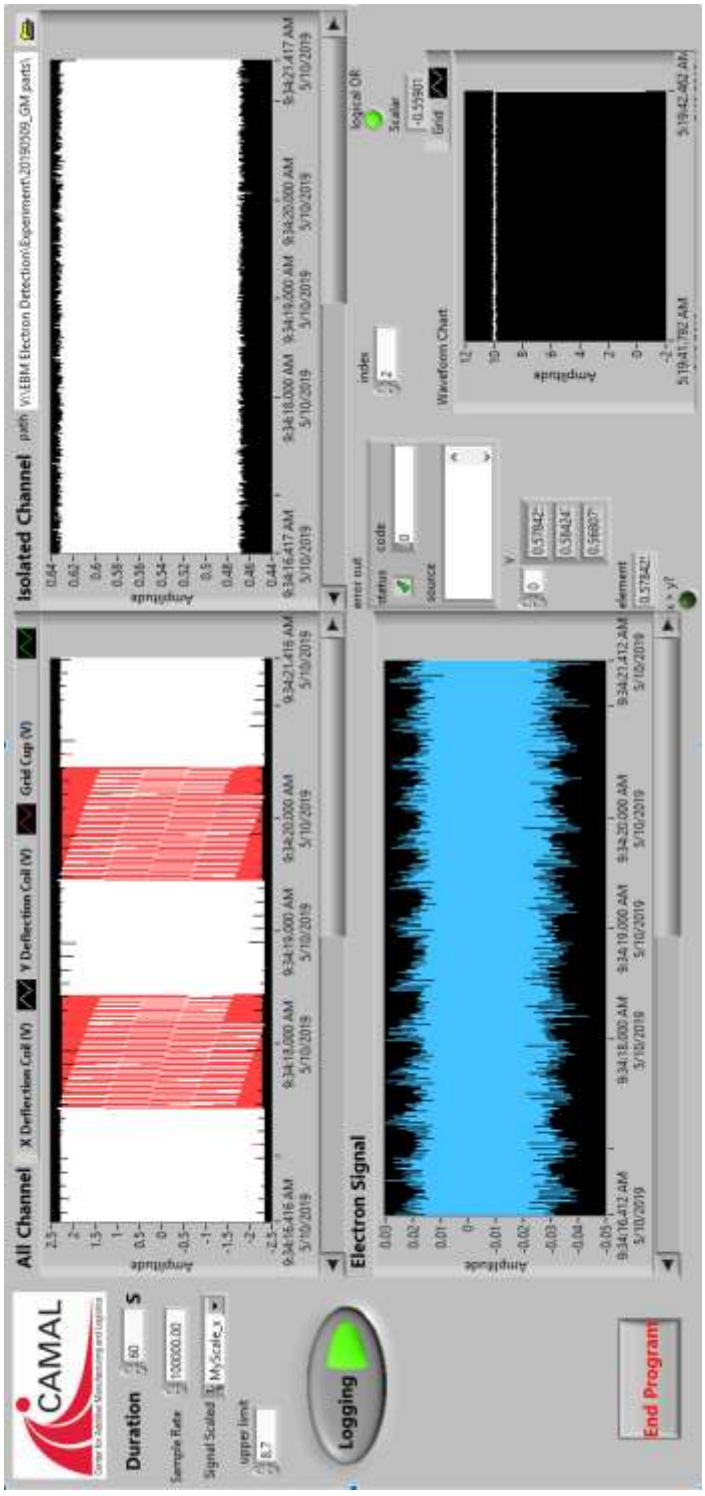

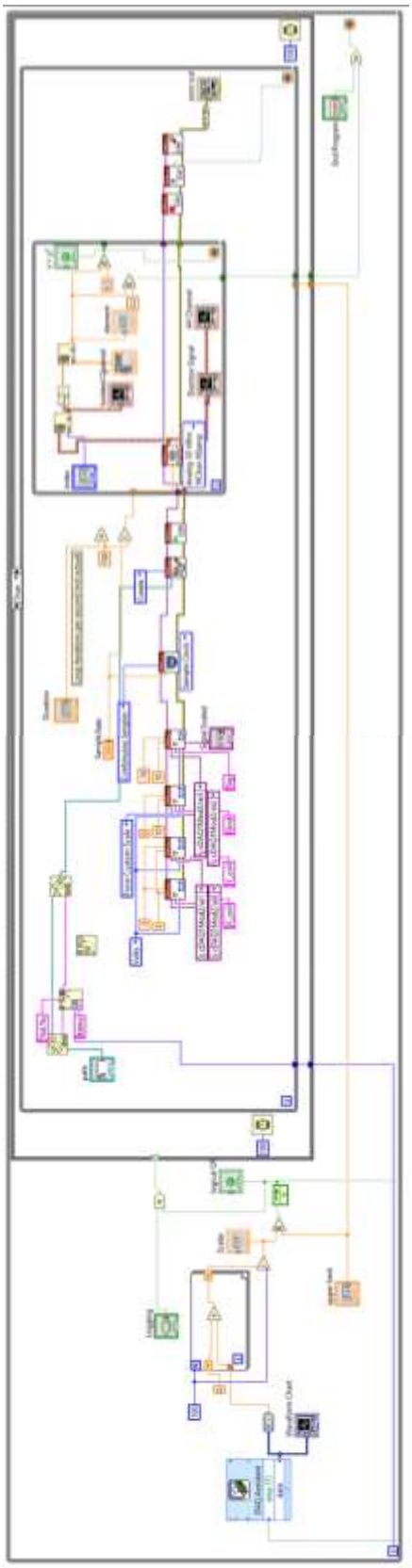

Appendix B

Code for automatic layer imaging

```
"""
Created on Mon Feb 25 15:00:11 2019
@author: mtung
"""

import os
import matplotlib.pyplot as plt
import numpy as np
from scipy import ndimage
from scipy import stats
from nptdms import TdmsFile
import re
import math

#Natural sorting
def atoi(text):
    return int(text) if text.isdigit() else text

def natural_keys(text):
    '''
    alist.sort(key=natural_keys) sorts in human order
    http://nedbatchelder.com/blog/200712/human_sorting.html
    (See Toothy's implementation in the comments)
    '''
    return [ atoi(c) for c in re.split(r'(\d+)', text) ]

def round_up(n, decimals=0):
    multiplier = 10 ** decimals
    return math.ceil(n * multiplier) / multiplier
```

```
path = os.getcwd()
folder_path = path


#The time frame to load the raw data, in 10μs
t1 = 700000
t2 = 3000000

# The mask for the XY range, XR for x axis right limit, XL for left, YT for y axis top limit, YB for bottom liimit
xR = 40
xL = -40
yT = 40
yB = 40

#Number of bins used for generate the image, depend on the XY range
binS = 40

#Mask for grid cup voltage upper and lower limits
gL = 6
gS = 4.8

#The amount of samples taken for speed calculation
j = 10

#Emptay array to store data if collecting value from a lot of files
p = []

#Directing the file OS to read only TDMS files
extensions = ('.tdms')

#The angle to rotate the image from the center, -0.06 is on;y for ARCAM A2
```

```
theta = -0.06
cos = np.cos
sin = np.sin

centerX = ((xR+xL)/2)
centerY = ((yT+yB)/2)

#Sequentially read files according to natural sort
for data_file in sorted(os.listdir(folder_path), key=natural_keys):

    #Getting the file name
    ext = os.path.splitext(data_file)[-1].lower()
    #Getting the file size
    sz = os.path.getsize(data_file)
    #Check if it's TDMS file
    if ext in extensions:
        #Check if the file is too small, if an error in DAQ accord it could record a super small file
        if (sz > 1000000):
            print (data_file)

            #Getting group name from the TDMS file
            tdms_file = TdmsFile('%s' % data_file)
            group_name = TdmsFile.groups(tdms_file)
            group_name1 = ''.join(group_name)

            #Assign array to the TDMS channels
            channel1 = tdms_file.object('%s' % group_name1, 'X_coil')
            x = channel1.data
            channel2 = tdms_file.object('%s' % group_name1, 'Y_coil')
            y = channel2.data
            channel3 = tdms_file.object('%s' % group_name1, 'Grid')
            g = channel3.data
```

```
channel4 = tdms_file.object('%s' % group_name1, 'Sig')
z = channel4.data
time = channel1.time_track()

#Mask the data by time fram, as well as converting them to mm
x = ((-1)*x[t1:t2])/0.042
y = y[t1:t2]/0.042
z = (z[t1:t2]*2)
g = g[t1:t2]
time = time[t1:t2]
#For speed calculation
dt = 1/(100000/j)

#Rotation
x = (x*cos(theta))-(y*sin(theta))
y = (y*cos(theta))+(x*sin(theta))
#Grid cup to current conversion
G = ((0.0517 * g * g * g * g) - (0.4729 * g * g * g) - (0.9561 * g * g) + (12.637 *g) - 2.2636)
#Correction from the input current and Log file relationship
G2 = ((-0.00002 * G * G * G * G) + (0.001 * G * G * G) - (0.0145 * g * g) + (0.0778 *g) - 0.1023)
G3 = G * (1 + (G2/100))

#Getting SEY
z2 = z/G3

#Mask by Grid cup contrrol voltage and XY limits
mask = ((g >= gS) & (g <= gL))
maskxy = (((x >= xL) & (x <= xR)) & ((y >= yB) & (y <= yT)))

#Beam Velocity calculation
speed = np.empty(len(x))
for i in range(len(x)):
```

```
    speed[i] = round_up(((math.sqrt(((x[i]-x[i-j])**2)+((y[i]-y[i-j])**2)))/dt),4)


    i = i+j


#Create a 2D array of the distance from the center of the XY limit
D = np.empty(len(x))
for i in range(len(x)):
    #D[i] = math.sqrt(((x[i]-centerX)**2)+((y[i]-centerY)**2))
    D[i] = abs(y[i]-centerY)


    i = i+j


#Getting Power
power =  60 * G3
PV = (power / speed)*1000


#Getting volume speed
vspeed = speed*0.04*0.1


#Speed image
H, xedges, yedges, binnumber = stats.binned_statistic_2d(x[mask & maskxy], y[mask & maskxy], values = vspeed[mask & maskxy], statistic='mean' , bins = [binS, binS])
XX, YY = np.meshgrid(xedges, yedges)


plt.style.use('classic')


fig = plt.figure(figsize = (12,10))
ax1 = plt.subplot(111)
ax1.tick_params(left=True, bottom=True, labelleft=True, labelbottom=True)
ax1.set_xlabel('mm',fontsize=20)
ax1.set_ylabel('mm',fontsize=20)
```

```
plot1 = ax1.pcolormesh(XX,YY,H.T, cmap='Greys_r', shading='flat',  vmin=0, vmax=20)

plt.axis([xL,xR,yB,yT])

plt.axes().set_aspect('equal', 'datalim')

cbar = plt.colorbar(plot1,ax=ax1, pad = .015, aspect=20)

cbar.ax.set_ylabel('(mm^3/s)' , rotation=90, fontsize=20)

#Put colorbar on the left, change 'pad' distance too

#cbar.ax.yaxis.set_ticks_position('left')

#plt.savefig('Vspeed_%s.png' % data_file)



#SET image

H2, xedges2, yedges2, binnumber = stats.binned_statistic_2d(x[mask & maskxy], y[mask & maskxy], values = z2[mask & maskxy], statistic='mean' , bins = [binS, binS])

XX2, YY2 = np.meshgrid(xedges2, yedges2)


plt.style.use('classic')


fig = plt.figure(figsize = (12,10))

ax1 = plt.subplot(111)

ax1.tick_params(left=True, bottom=True, labelleft=True, labelbottom=True)

ax1.set_xlabel('mm',fontsize=20)

ax1.set_ylabel('mm',fontsize=20)

plot1 = ax1.pcolormesh(XX2,YY2,H2.T, cmap='Greys_r', shading='flat',  vmin=0, vmax=0.5)


plt.axis([xL,xR,yB,yT])

plt.axes().set_aspect('equal', 'datalim')


cbar = plt.colorbar(plot1,ax=ax1, pad = .015, aspect=20)

cbar.ax.set_ylabel('(SEY)' , rotation=90, fontsize=20)

#cbar.ax.yaxis.set_ticks_position('left')

#plt.savefig('SEY_%s.png' % data_file)
```

```
#Power image
H1, xedges1, yedges1, binnumber = stats.binned_statistic_2d(x[mask & maskxy], y[mask & maskxy], values = power[mask & maskxy], statistic='mean' , bins = [binS, binS])
XX1, YY1 = np.meshgrid(xedges1, yedges1)

plt.style.use('classic')

fig = plt.figure(figsize = (12,10))
ax1 = plt.subplot(111)
ax1.tick_params(left=True, bottom=True, labelleft=True, labelbottom=True)
ax1.set_xlabel('mm',fontsize=20)
ax1.set_ylabel('mm',fontsize=20)
plot1 = ax1.pcolormesh(XX1,YY1,H1.T, cmap='Greys_r', shading='flat',  vmin=0, vmax=800)

plt.axis([xL,xR,yB,yT])
plt.axes().set_aspect('equal', 'datalim')
cbar = plt.colorbar(plot1,ax=ax1, pad = .015, aspect=20)
cbar.ax.set_ylabel('(W)' , rotation=90, fontsize=20)
#cbar.ax.yaxis.set_ticks_position('left')
#plt.savefig('Power_%s.png' % data_file)

#Distance to center
H3, xedges3, yedges3, binnumber = stats.binned_statistic_2d(x[mask & maskxy], y[mask & maskxy], values = D[mask & maskxy], statistic='mean' , bins = [binS, binS])
XX3, YY3 = np.meshgrid(xedges3, yedges3)

plt.style.use('classic')

fig = plt.figure(figsize = (12,10))
ax1 = plt.subplot(111)
ax1.tick_params(left=True, bottom=True, labelleft=True, labelbottom=True)
```

```
        ax1.set_xlabel('mm',fontsize=20)
        ax1.set_ylabel('mm',fontsize=20)

        plot1 = ax1.pcolormesh(XX3,YY3,H3.T, cmap='Greys_r', shading='flat',  vmin=0, vmax=6)
        plt.axis([xL,xR,yB,yT])
        plt.axes().set_aspect('equal', 'datalim')
        cbar = plt.colorbar(plot1,ax=ax1, pad = .015, aspect=20)
        cbar.ax.set_ylabel('(mm)' , rotation=90, fontsize=20)
        #cbar.ax.yaxis.set_ticks_position('left')
        #plt.savefig('Power_%s.png' % data_file)

        S = np.ravel((H.T))
        A = np.ravel((H1.T))
        E = np.ravel((H2.T))
        D1 = np.ravel((H3.T))

        np.savetxt('2-2_Vspeed.txt',(S))
        np.savetxt('2-2_Power.txt',(A))
        np.savetxt('2-2_edge.txt',(D1))

        plt.show()

        '''
        #Emptay array to store data if collecting value from a lot of files
        Avg = np.mean(speed[mask & maskxy])
        print(Avg)
        p.append(Avg)
        '''

#np.savetxt('_speed.txt', np.c_[p])
```

Appendix C

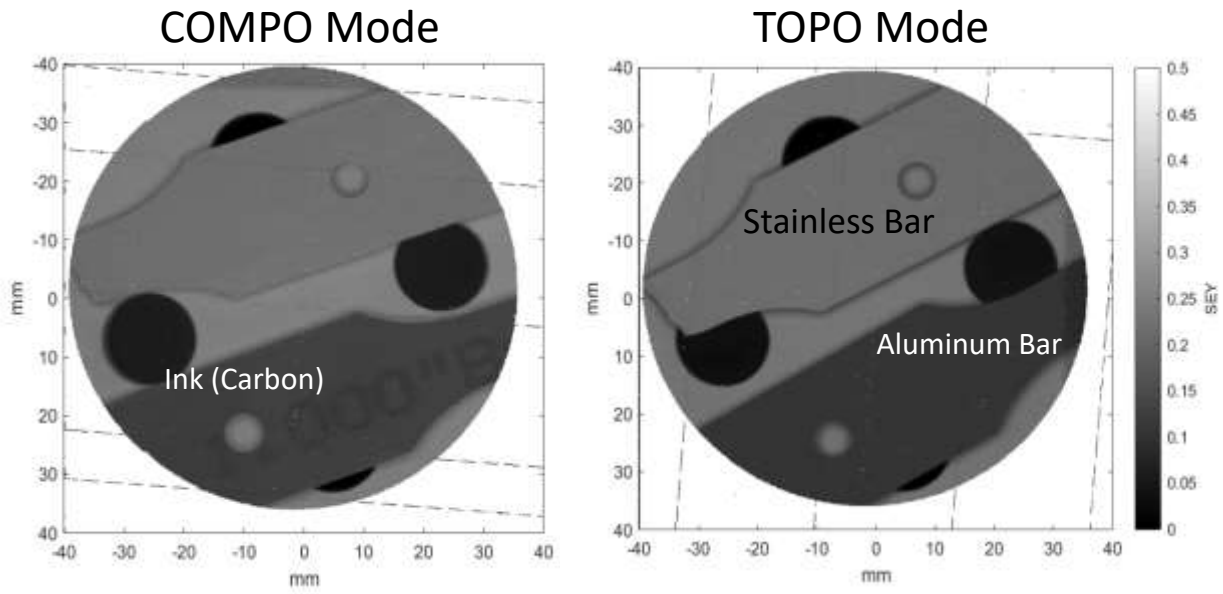
COMPO Mode
TOPO Mode
Ink (Carbon)
Stainless Bar
Aluminum Bar
mm
SEY